STUDY ON GROUND BASED SYNTHETIC APERTURE RADAR SIGNAL PROCESSING AND INTERFEROMETRY FOR CHANGE DETECTION

by

Güneycan Kılıç

B.S., Electrical-Electronics Engineering, Boğaziçi University, 2017

Submitted to the Institute for Graduate Studies in

Science and Engineering in partial fulfillment of

the requirements for the degree of

Master of Science

Graduate Program in Electrical-Electronics Engineering

Boğaziçi University

2020

ACKNOWLEDGEMENTS

ABSTRACT

STUDY ON GROUND BASED SYNTHETIC APERTURE RADAR SIGNAL PROCESSING AND INTERFEROMETRY FOR CHANGE DETECTION

In this study, a ground based synthetic aperture radar system is designed to collect the experimental data for monitoring the target region, form indoor and outdoor two dimensional radar images, compare two radar images received at different times and detect potential changes and movements of the objects by using radar interferometry.

Ground-based synthetic aperture radar interferometry is a powerful tool to receive the velocity field of the target region, compare two radar images and calculate the displacements of the objects in the target region. In the interferometric phase image, the large phase differences or the discontinuities between consecutive pixels are eliminated to reconstruct the true profile and reduce the effect of the local errors by using two dimensional phase unwrapping algorithm. Also, atmospheric and instrumental decorrelation sources are excluded to correct phase and displacement measurements in the radar interferometry. Finally, the true phase changes and the actual displacements are received.

An application of ground-based synthetic aperture radar interferometry is analyzed and discussed in this study. Results show that the proposed method on ground-based synthetic aperture radar is a valid alternative to spaceborne and airborne synthetic aperture radar interferometry.

ÖZET

DEĞİŞİKLİK ALGILAMA İÇİN YAPAY AÇIKLIK RADAR SİNYAL İŞLEME VE GİRİŞİMÖLÇME ÜZERİNE BİR ÇALIŞMA

Bu çalışmada hedef alanın deney verisini toplamak, binanın içerisinde ve dışarısında iki boyutlu radar imgesi oluşturmak, farklı zamanlarda elde edilmiş iki radar imgesini karşılaştırmak ve radar girişimölçer kullanarak nesnelerin hareketlerini, değişiklikleri tespit etmek için yer tabanlı yapay açıklık radar sistemi geliştirilmiştir.

Hedef alanı ve değişimi görüntülemek, iki radar imgesini karşılaştırmak ve nesnelerin yer değişimlerini hesaplamakiçin yer tabanlı yapay açıklık radar girişimölçer güçlü bir araçtır. Gerçek profili inşaa etmek, yerel hata etkisini azaltmak için iki boyutlu evre düzenlemesi algoritması kullanılarak komşu pikseller arasındaki geniş evre farkları ve süreksizlikler elimine edilmiştir. Ayrıca, radar girişimölçerdeki evre ölçümlerini düzeltmek için atmosferik ve aygıtsal dekorelasyon kaynakları çıkartılmıştır. Sonunda, gerçek yer ve evre değişimlerine ulaşılmıştır.

Bu çalışmada yer tabanlı yapay açıklık radarın bir uygulaması incelenmiş ve tartışılmıştır. Sonuçlar yer tabanlı yapay açıklık radar üzerine önerilen bu yöntemin uzay ve hava tabanlı yapay açıklık radar girişimölçerleriyle birlikte geçerli bir seçenek olduğunu göstermiştir.

TABLE OF CONTENTS

LIST OF FIGURES

LIST OF TABLES

LIST OF SYMBOLS

A_w	Effective antenna aperture
B	Bandwith
c	Speed of light in air
$d(l_n, p_m)$	Distance between the scatterer and the transceiver
f_a	Frequency level in the calibration
f_c	Centre frequency
G	Antenna gain
I	Identity matrix
L	Aperture length
L_{ges}	Loss factor
l_n	Position of the transmitting/receiving antennas on the moving rail
M	Total number of pixels in the target region
N	Azimuth point numbers
P_e	Received power
p_m	Position of the scatterer that is at the centre of each pixel
P_r	Reflected power
P_s	Transmitted power
R	Slant range
r_1	Range of the object in the master image of radar interferometry
r_2	Range of the object in the slave image of radar interferometry
R_1	Range from transmitting antenna
R_2	Range to receiving antenna
R_{na}	Non ambigous range
S	Matrix for measured S_{21} parameters
S_{21}	Description of S_{21} parameters
S_e	Power density at the receiving antenna

S_g	Directional power density
S_u	Nondirectional power density
t	Time
Z	Matrix for $z(f_a, l_n, p_m)$ calculations
α_f	Range dependent coefficient for instrumental instability
β_φ	Range dependent coefficient for instrumental instability
Δf	Frequency step
Δr	Displacement
ΔR	Range resolution
$\Delta \vartheta$	Azimuth resolution
ϵ_{atm}	Drift in the atmospheric refractivity
ϵ_f	Drift of the centre frequency
γ	Characteristic of the scatterer at the centre of a cell
Γ	Matrix for the characteristics of the scatterers at the centre of each cell
κ	Tikhonov Regularization coefficient
λ	Wavelength
λ_c	Centre wavelength
σ	Radar cross section
τ	Time delay
φ	Interferometric phase

LIST OF ACRONYMS/ABBREVIATIONS

2D	Two Dimensional
GB-SAR	Ground-Based Synthetic Aperture Radar
RCS	Radar Cross Section
SAR	Synthetic Aperture Radar
SNR	Signal-to-Noise Ratio
VNA	Vector Network Analyzer

1. INTRODUCTION

Radar is the acronym for "radio detection and ranging" and the main objective of the radar is measuring the range, direction and velocity of the objects. Radar systems are developed to be used in military and civil applications [1]:

- surveillance
- air-policing
- missile control
- weapon control
- navigation
- air traffic
- weather
- speed gauges
- cruise control
- reasearch

The radar systems have the capability of detecting and tracking objects. Radar echoes become useful by analyzing transmitted and received signals and then evaluating the travel time of their round trip, since the electromagnetic signals propagate through the atmosphere with high gain despite the clouds, weather condition and aoresols [2]. There are many constraints that effect the performance of the radar systems, such as average power, antenna gain, antenna aperture, physical size of the antenna, operation frequency, and hardware limitations.

Since radar echoes carry amplitude and phase information, the pixels of the resulting radar image are complex numbers. The amplitude of a pixel in the radar image corresponds to the reflectivity or the incident energy sent back to the receiving antenna of the radar system. For example, trees have small reflectivity in the nature but metallic objects send back greater energy and have higher reflectivity. The phases of

the pixels in the radar image records many different effects and become meaningful when it is compared with another radar image.

Ground-based synthetic aperture radar (GB-SAR) systems and devices are generally used for indoor and outdoor two dimensional (2D) radar imaging applications. The phase difference between two successive radar images gives the interferometric phase image of GB-SAR [3]. GB-SAR interferometry is an accomplished method to compare two radar images, which are taken at different times, of the predetermined target region, monitor displacements, detect changes. GB-SAR interferogram shows the velocity field of the objects in the target region [4]. The phase information of a pixel in the interferogram is directly related to the displacement in the range direction of the pixel. The phases in the radar interferometry should be analyzed to evaluate the geometric differences.

2D phase unwrapping is a successful method to reach the true profile of the GB-SAR interferogram because the phases in the interferogram are only measured modulo 2π [5]. Since phase is continuous, the absolute phase difference between two consecutive pixels in the radar interferometry should be less than π [5]. If the phase difference between the pair of neighboring pixels is more than π, there is a discontinuity in the interferometry [6]. These artifacts between consecutive pixels should be eliminated as possible. The main method of the phase unwrapping algorithm is to reconstruct the GB-SAR interferogram by adding multiple of the period, 2π, to the interferometric phases of necessary pixels [5].

Since the phase difference between two successive radar images gives the GB-SAR interferometric phase image, interferogram is retrieved from the conjugate product of two GB-SAR images [3]. Receiver thermal noise, instrumental noise and atmospheric delay are the major sources of mismeasurements in the radar interferometry. Some specific algorithmic tools are needed for filtering, reducing the effect of noise and reaching the true results. To correct measured phases and displacements, permanent scatterers such as steady rocks or boulders are used or steady objects with high reflectivity are

located as reference points in the target region during the measurements since their displacements should be equal to zero [7].

Following the instruction, data acquisition method and GB-SAR system are expressed. Then two radar imaging algorithms are identified, radar interferometry and algorithms for diagnosing errors and extracting their effect are explained in the next chapter. Finally, radar images and interferometric results are obtained and some conclusions are shared.

1.1. Fundamentals of Radar

Invention and development of the radar systems is a process starting from usage of electromagnetic signals. There are many important milestones in the process of improvement of the radar systems:

- In 1865, James Clerk Maxwell proved that electromagnetic signals travel through space at the constant speed of light [8].
- In 1904, Christian Hulsmeyer invented telemobiloscope to control sea traffic by using reflections of electromagnetic signals and detected metallic objects [8].
- In 1910, an early form of magnetron was invented by H. Gerdien. In 1921, Albert Hull invented the split-anode magnetron to detect objects at longer ranges [8].
- In 1936, the radar system 'klystron' with higher power was invented [8].
- During the World War II and Cold War Germany, United States of America, England, France and Russia developed military radar systems [8].
- In 1951, Carl A. Wiley invented synthetic aperture radar (SAR). [8]
- Today, many countries make important investments to develop military and civil radar systems with higher performance [8].

An electromagnetic signal, which is emitted by the radar system, is either reflected back by an object and turns back to the radar system or scatters to the air. The working principle of the radar systems is calculating the distance of the reflective object using

time delay between transmitted signal and received signal [9].
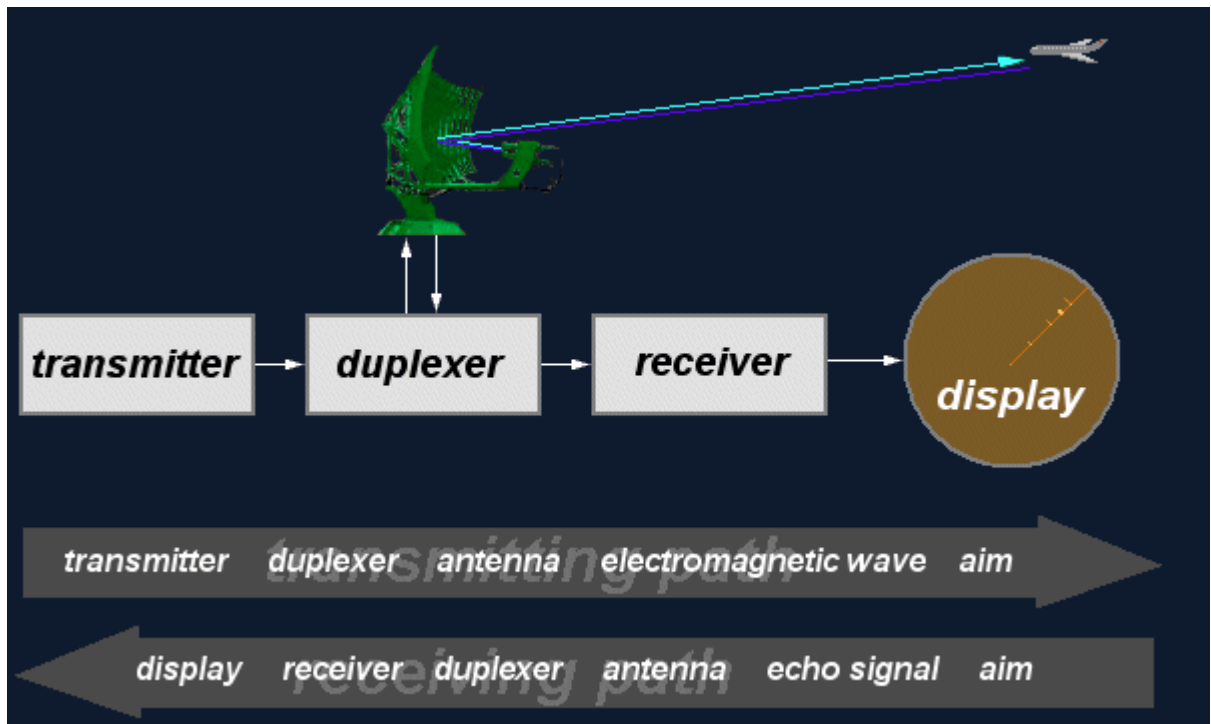
Figure 1.1. Block diagram of radar operating concept [9].

Antennas convert the electrical signal into radio waves or radio waves into electrical signal. In radar systems, active antennas are preferred generally. Transmitting antenna generates electromagnetic signals and the signal may be pulsed or continuous wave shape. Receiving antenna acquires the electromagnetic signal, which is reflected back by an object, and filters out the noise component of the signal. Additional power amplifier might be involved in transmitter and receiver.

Operating frequency of the radar system depends on application areas and hardware requirements, such as antenna size. The sizes of the components of the radar systems determines the mobility of the radar system and the mobility of the radar system affects the operating frequency range [10]. Radar systems can also be specified with respect to their operating frequency range [11]:

- HF-VHF Radar: The frequency range is from 3 MHz to 300 MHz. Physically larger antennas must be built to work with these wavelengths, so the frequency

range is not suitable for mobile radar systems. HF-VHF radar systems are used for early warning systems [12].

- UHF Radar: The frequency range is from 300 MHz to 3 GHz. UHF radar systems are used for detection and tracking over a long range [12].
- L-Band Radar: The frequency range is from 1 GHz to 2 GHz. L-band radar systems are used for detection and tracking over a range of 400 km [12].
- S-Band Radar: The frequency range is from 2 GHz to 4 GHz [12].
- C-Band Radar: The frequency range is from 4 GHz to 8 GHz. Relatively small antennas are used to work with these wavelengths. The frequency range is suitable for mobile radar systems and SAR applications [12].
- X-Band Radar: The frequency range is from 8 GHz to 12 GHz [12].
- Ku-Band Radar: The frequency range is from 12 GHz to 18 GHz. X and Ku-band radar systems are used in missile guidance applications [12].
- K-Band Radar: The frequency range is from 18 GHz to 27 GHz [12].
- Ka-Band Radar: The frequency range is from 27 GHz to 40 GHz. K and Ka-band radar systems are used in automatic take-off and landing systems of aircrafts and missile guidance applications [12].
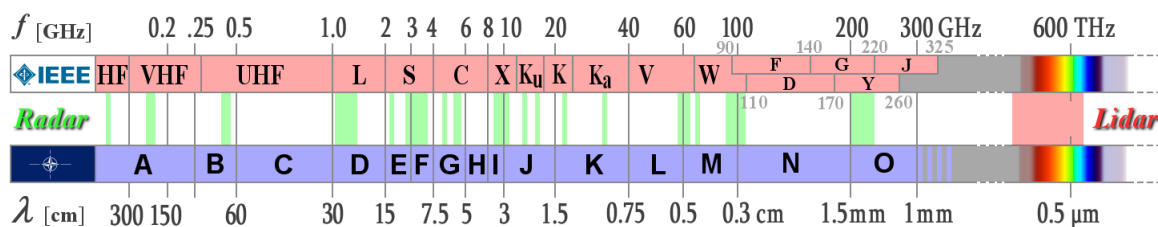
Figure 1.2. Frequency spectrum of radar systems [12].

The radar range equation gives the physical dependencies of the slant range R, transmitted power P_s, received power P_e, radar cross section (RCS) σ [13]. RCS is the measure of the ability of the target to reflect back electromagnetic signal to the receiving antenna. Projected cross section, reflectivity and the directivity are the factors that affect the RCS [14].

Figure 1.3. Trihedral corner reflectors.

In the measurement setup, two trihedral corner reflectors, whose one side of the length is 25 cm, with high RCS are generally placed across the GB-SAR system. RCS of a trihedral corner reflector is given by [15]

$$\sigma = \frac{12\pi a^4}{\lambda} \tag{1.1}$$

where λ is wavelength and a is the length of a side of the trihedral corner reflector.

The radar range equation determines the maximum range, which can be achieved by the radar system, and the maximum range determines the performance of the radar system.

If an isotropic radiator emits electromagnetic signal, the energy spreads out uniformly in all directions. The surface area of a sphere with radius R is $4\pi R^2$,

$$S_u = \frac{P_s}{4\pi R_1^2} \tag{1.2}$$

where S_u is nondirectional power density and R_1 is the range from transmitting antenna. Then the transmitted power in all directions is canalized into one direction and

the power density increases in the direction of the radiation,

$$S_g = S_u G \tag{1.3}$$

where S_g is directional power density and G is the antenna gain. The target detection also depends on the reflected power,

$$P_r = S_g \sigma \tag{1.4}$$

where P_r is reflected power, and

$$P_r = \frac{P_s}{4\pi R_1^2} G\sigma \tag{1.5}$$

$$S_e = \frac{P_r}{4\pi R_2^2} \tag{1.6}$$

where S_e is the power density at the receiving antenna and R_2 is the range to receiving antenna, and

$$P_e = S_e A_w \tag{1.7}$$

where A_w is effective antenna aperture.

$$P_e = \frac{P_r}{4\pi R_2^2} A_w \tag{1.8}$$

$$P_e = \frac{\frac{P_s}{4\pi R_1^2} G\sigma}{4\pi R_2^2} A_w \tag{1.9}$$

$$P_e = \frac{P_s G \sigma}{4\pi^2 R_1^2 R_2^2} A_w \tag{1.10}$$

Since $R_2 \approx R_1 = R$, and G is given by,

$$G = \frac{4\pi A_w}{\lambda^2} \tag{1.11}$$

$$P_e = \frac{P_s G^2 \sigma \lambda^2}{4\pi^3 R^4} \tag{1.12}$$

$$R = \sqrt[4]{\frac{P_s G^2 \sigma \lambda^2}{P_e 4\pi^3}} \tag{1.13}$$

Internal attenuation factors on transmitting and receiving paths, fluctuations after reflection and atmospheric state reduce the performance of the radar system [13]. After these sources are taken into consideration, the radar range equation finally becomes

$$R = \sqrt[4]{\frac{P_s G^2 \sigma \lambda^2}{P_e 4\pi^3 L_{ges}}} \tag{1.14}$$

where L_{ges} is loss factor.

1.2. Synthetic Aperture Radar

As mentioned earlier, antenna aperture effects the performance of the radar systems. As antenna aperture gets larger, the performance and the maximum range for detection increases in conventional radar systems. SAR systems don't need large antennas for radar imaging applications and relatively small antennas are used since the radar platform is able to move in azimuth direction [16].
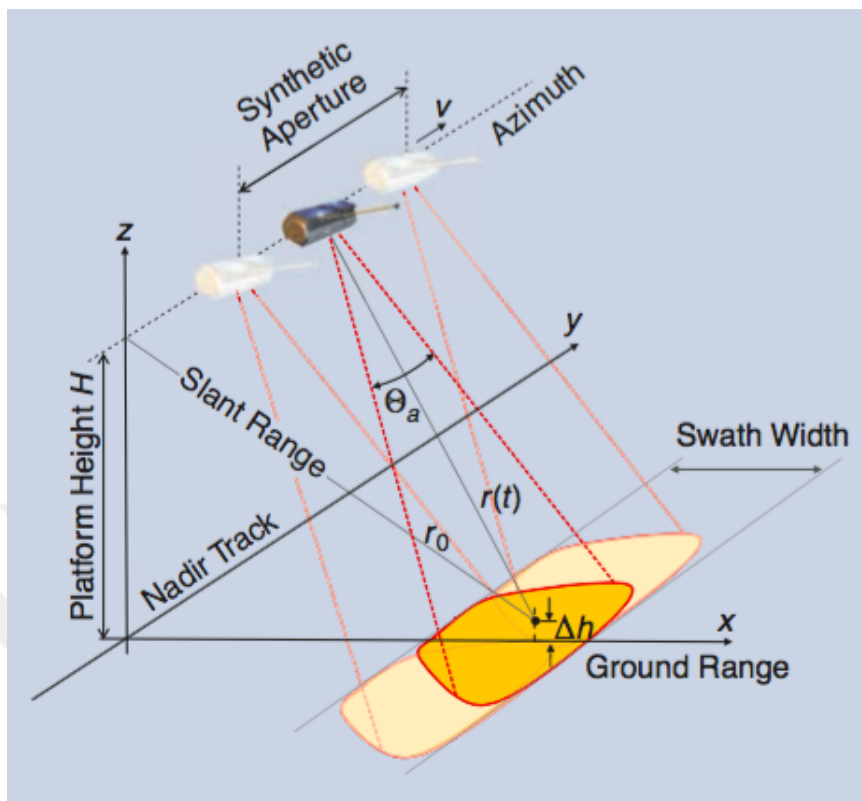
Figure 1.4. Airborne SAR [2].

After electromagnetic signals are transmitted and received back by the antennas in the SAR systems, the radar platform moves to next position and the transmitting antenna again emits electromagnetic signals and the receiving antenna collects the radar echoes. Since the SAR system is able to receive reflected radar signals in different positions, it constructs a virtual aperture length, that is larger than the physical aperture length, and gives a finer spatial resolution than conventional beam-scanning radars over a target region [17].

SAR is used to construct 2D radar images. 2D SAR images are the mapping of the received electromagnetic signal energy in range and azimuth directions [18].

2. 2D GROUND BASED SYNTHETIC APERTURE RADAR IMAGING

A GB-SAR system is designed to collect the S_{21} parameters of the target region and a novel 2D GB-SAR imaging algorithm is developed to monitor the target area. The GB-SAR platform consists of a computer, a transmitting antenna, a receiving antenna, and a vector network analyzer (VNA). They are positioned on the rail, which has a length of 2 meters. The system is shown in Figure 2.1. The computer controls both the rail and the VNA. After VNA collects the S_{21} parameters of the environment and sends to the computer, the radar platform, which is at the beginning of the rail, moves 20 mm in azimuth direction and the VNA repeats the same procedure. This process continues until the platform reaches to the end of the rail.
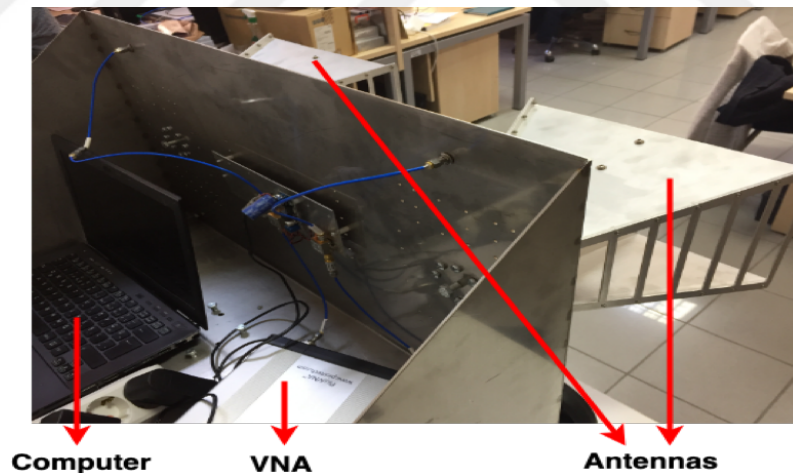
Figure 2.1. GB-SAR system equipments (computer, VNA, and antennas on the linear rail.)

VNA and antennas are calibrated in 201 steps in C-band to increase resolution and the bandwidth is determined as 1 GHz and the frequency step is 5 MHz. The transmitter sends infinite number of electromagnetic signals for calibrated frequencies in all directions and some of those infinite number of signals are reflected back to the receiver from scatterers with time delay. As mentioned before, S_{21} parameters of the environment are collected each time after the platform moves 20 mm. Finally, a

201×101 matrix is received.

The target region is divided into pixels and the the number of the scatterers is M. l_n denotes the position of the transceiver on the moving rail, p_m denotes the position of the scatterer, that is at the centre of each cell, and $d(l_n, p_m)$ denotes the distance between the scatterer and the transceiver. The center of the rail is accepted as the origin, $(0,0)$, the coordinates of l_0 is $(-1,0)$ and the coordinates of l_{100} is $(1,0)$. The structure is visualized in Figure 2.2.
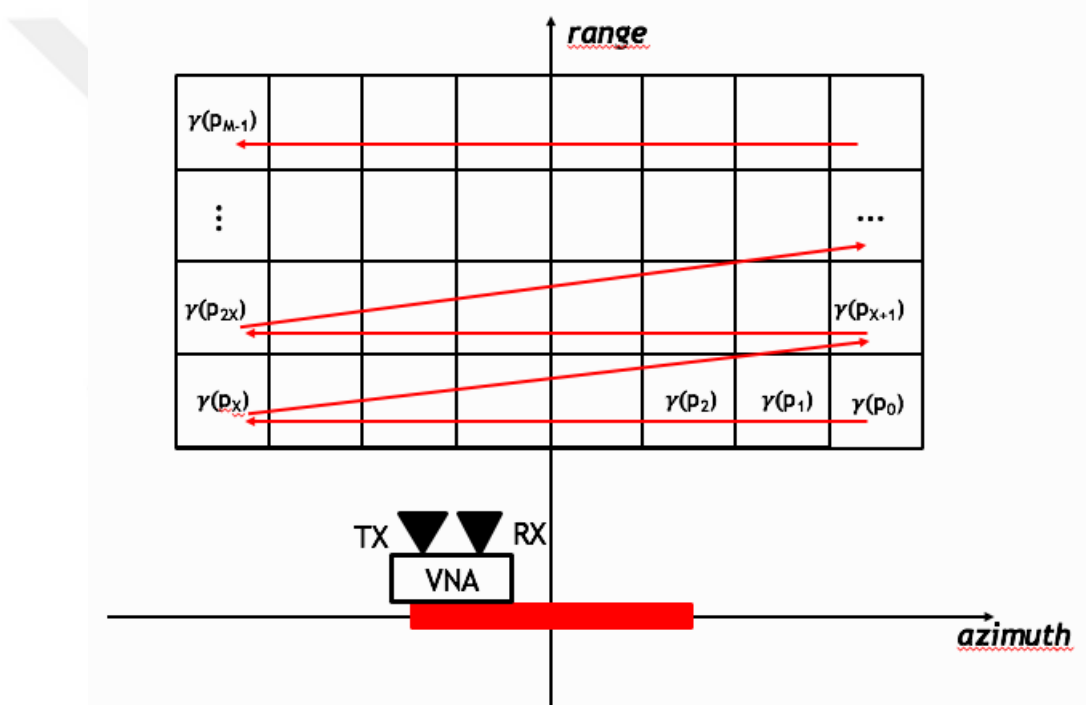
Figure 2.2. Target region as grid and GB-SAR system on the rail (x corresponds to azimuth direction and y corresponds to range direction).

The transmitting antenna sends complex sinusoidal signal $exp(j2\pi f_a t)$ and the signal is reflected back by the scatterer. The receiving antenna observes this signal as

$$\gamma(p_m)exp(j2\pi f_a(t - \tau)) \tag{2.1}$$

where τ is time delay and $\gamma(p_m)$ is the characteristic of the scatterer at the centre of a cell.

VNA provides S_{21} parameter for a single frequency at the given location of the moving rail as the sum of the ratio of the received signals, which are reflected back, and their corresponding transmitted signals. Since the target region is divided into M cells or pixels and there is a scatterer at the centre of each pixel, each scatterer reflects back an electromagnetic signal and number of the received back signals for a single frequency at the given location of the moving rail is equal to number of the scatterers.

$$S_{21}(f_a, l_n) = \sum_{m=0}^{m=M-1} \frac{\gamma(p_m)exp(j2\pi f_a(t-\tau))}{exp(j2\pi f_a t)} \tag{2.2}$$

The ratio of the received signal and transmitted signal in equation 2.2 can be represented as,

$$\frac{\gamma(p_m)exp(j2\pi f_a(t-\tau))}{exp(j2\pi f_a t)} = exp(-j2\pi f_a \tau)\gamma(p_m) \tag{2.3}$$

Then equation 2.2 becomes,

$$S_{21}(f_a, l_n) = \sum_{m=0}^{m=M-1} exp(-j2\pi f_a \tau)\gamma(p_m) \tag{2.4}$$

Time delay is equal to $2d(l_n, p_m)/c$ and c denotes the speed of light,

$$S_{21}(f_a, l_n) = \sum_{m=0}^{m=M-1} exp(-j2\pi f_a \frac{2d(l_n, p_m)}{c})\gamma(p_m) \tag{2.5}$$

Then z parameter of the scatterer for a single frequency at the given location of the moving rail is defined as,

$$z(f_a, l_n, p_m) = exp(-j2\pi f_a \frac{2d(l_n, p_m)}{c}) \tag{2.6}$$

Then equation 2.4 becomes,

$$S_{21}(f_a, l_n) = \sum_{m=0}^{m=M-1} z(f_a, l_n, p_m)\gamma(p_m) \tag{2.7}$$

Equation 2.7 can be represented by using matrices,

$$\begin{bmatrix} S_{21}(f_0, l_0) \\ \vdots \\ S_{21}(f_0, l_{100}) \\ S_{21}(f_1, l_0) \\ \vdots \\ S_{21}(f_{200}, l_{100}) \end{bmatrix} = \begin{bmatrix} z(f_0, l_0, p_0) & \cdots & z(f_0, l_0, p_{M-1}) \\ \vdots & \ddots & \vdots \\ z(f_0, l_{100}, p_0) & \cdots & z(f_0, l_{100}, p_{M-1}) \\ z(f_1, l_0, p_0) & \cdots & z(f_1, l_0, p_{M-1}) \\ \vdots & \ddots & \vdots \\ z(f_{200}, l_{100}, p_0) & \cdots & z(f_{200}, l_{100}, p_{M-1}) \end{bmatrix} \begin{bmatrix} \gamma(p_0) \\ \gamma(p_1) \\ \vdots \\ \gamma(p_{M-1}) \end{bmatrix}$$

$S = Z\Gamma$ and S matrix correspond to S_{21} parameters that are measured by VNA and the numbers in the Z matrix is calculated using equation 2.6. The unique solution for Γ matrix is found by employing Tikhonov regularization because Tikhonov regularization is applied for ill-posed inverse problems in order to stabilize the solution [19].

$$\Gamma = (\kappa I + Z^H Z)^{-1} Z^H S \tag{2.8}$$

κ is accepted as 200 to calculate scatterer characteristics. If a small value for κ is chosen, the instability continues, whereas too large value for κ results in an overregularized stable solution [20]. If the true solution for Γ matrix is a priori, an optimal choice for κ can be found by minimizing the relative error. Result of the delay-and-sum algorithm, which will be explained in the next section, can be accepted as the true solution. After the amplitude of each scatterer is calculated, 2-D radar image is constructed.

2.1. Delay-and-Sum Algorithm

Delay-and-sum algorithm is one of the most well-known and widely-used method for 2D GB-SAR imaging. Delay-and-sum algorithm have the same structure to form 2D radar images but matrix operations are not needed in delay-and-sum method and this algorithm reduces the computational burden via some mathematical manipulations.

Since they have the same initial structure, VNA provides S_{21} parameter for a single frequency at the given location of the moving rail as the sum of the ratio of the received signals, which are reflected back, and their corresponding transmitted signals. Since the target region is divided into M cells or pixels and there is a scatterer at the centre of each pixel, each scatterer reflects back an electromagnetic signal and number of the received back signals for a single frequency at the given location of the moving rail is equal to number of the scatterers. Equation 2.5 is manipulated to find the sum of the all S_{21} parameters,

$$\sum_{a=0}^{a=200} \sum_{n=0}^{n=100} S_{21}(f_a, l_n) = \sum_{a=0}^{a=200} \sum_{n=0}^{n=100} \sum_{m=0}^{m=M-1} exp(-j2\pi f_a \frac{2d(l_n, p_m)}{c})\gamma(p_m) \qquad (2.9)$$

Then both sides of the equation are multiplied with $exp(j2\pi f_a 2d(l_n, p_k)/c)$ and the left side of the equation 2.9 becomes,

$$\sum_{a=0}^{a=200} \sum_{n=0}^{n=100} \sum_{k=0}^{k=M} S_{21}(f_a, l_n) exp(j2\pi f_a \frac{2d(l_n, p_k)}{c}) \qquad (2.10)$$

The right side of the equation 2.9 becomes,

$$\sum_{a=0}^{a=200} \sum_{n=0}^{n=100} \sum_{m=0}^{m=M-1} \sum_{k=0}^{k=M-1} exp(-j2\pi f_a \frac{2d(l_n, p_m)}{c}) exp(j2\pi f_a \frac{2d(l_n, p_k)}{c})\gamma(p_m) \qquad (2.11)$$

Then equation 2.10 and 2.11 becomes,

$$\sum_{a=0}^{a=200} \sum_{n=0}^{n=100} S_{21}(f_a, l_n) exp(j2\pi f_a \frac{2d(l_n, p_m)}{c}) = \gamma(p_m) \sum_{a=0}^{a=200} \sum_{n=0}^{n=100} 1 \qquad (2.12)$$

Equation 2.12 can be easily converted into,

$$\frac{\sum_{a=0}^{a=200} \sum_{n=0}^{n=100} S_{21}(f_a, l_n) exp(j2\pi f_a \frac{2d(l_n, p_m)}{c})}{201 \times 101} = \gamma(p_m) \qquad (2.13)$$

After the amplitude of each scatterer is calculated, 2-D radar image is constructed [21].

3. RADAR INTERFEROMETRY

Radar echo is a complex number and has an amplitude and a phase. The amplitude of the pixel in the radar image corresponds to reflectivity [22]. The phases of the pixels get meaningful when two radar images are compared. The difference of phases of two radar images is called interferogram [3]. The radar interferometry is an accomplished method to detect changes between two radar images taken at different times and monitor velocity field of the objects in the target region. The interferometric phase image is directly related to the displacement of the objects in the range direction when two radar images are compared. GB-SAR interferometry is able to retrieve displacements, which cannot be measured by airborne radar.

The radar image obtained with the first dataset is accepted as the master image, the radar image obtained with the second dataset is accepted as slave image and the slave image is mapped onto the master image to evaluate the geometric differences between the two radar images [22]. Both of the radar images are obtained by using delay-and-sum method. $\gamma(p_{m,1})$ denotes the characteristic of the scatterer at the centre of mth pixel of the master image, $\gamma(p_{m,2})$ denotes the characteristic of the scatterer at the centre of mth pixel of the slave image and both $\gamma(p_{m,1})$ and $\gamma(p_{m,2})$ are complex numbers as mentioned before. The value at the mth pixel of the the interferometric phase image, φ_m, is evaluated,

$$\varphi_m = \angle \gamma(p_{m,1}) \gamma(p_{m,2})^*$$ (3.1)

where the asterisk denotes the complex conjugation. The interferometric phase φ_m is translated into the displacement in the mth pixel Δr_m by means of the relationship [23],

$$\Delta r_m = \frac{c}{4\pi f_c} \varphi_m$$ (3.2)

where f_c is centre frequency and is equal to the average of f_0 and f_{200}, and

$$\lambda_c = \frac{c}{f_c} \qquad (3.3)$$

where λ_c is the centre wavelength.

$$\Delta r_m = \frac{\lambda_c}{4\pi} \varphi_m \qquad (3.4)$$
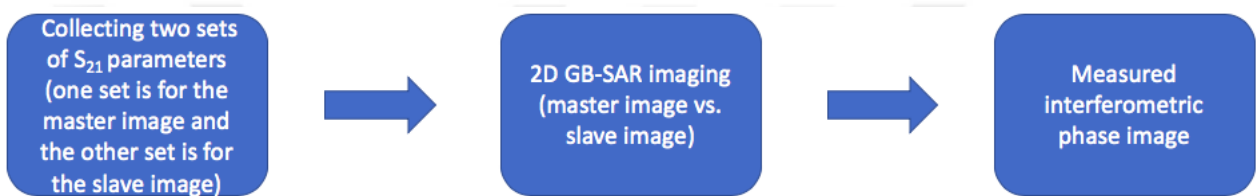
Figure 3.1. Block diagram for radar interforemetry.

3.1. 2D Phase Unwrapping

2D phase unwrapping is a specific algorithm to receive the true profile of the target region, correct the local errors where a few pixels are corrupted because these local errors can propagate to global phase and displacement errors in the entire image [24]. Interferometric phases are needed to obtain elevations to detect displacements larger than $(\frac{\lambda_c}{4\pi}\pi)$ in the pixels since the range of the interferometric phase of a pixel is from $-\pi$ to π and the phases in the interferogram are only measured modulo 2π [24].

Phase should be continuous, so the absolute phase difference between two neighboring pixels in the radar interferogram should be less than π [5]. A discontinuity occurs in the interferogram if the phase difference between a pair of consecutive pixels is more than π [6]. The objective of phase unwrapping is to minimize the number of discontinuities and remove all of them.

The main method of the phase unwrapping algorithms is to reconstruct the interferometric phase image by adding multiples of the period, 2π, to the necessary pixels

[5].

$$\hat{\varphi}_{x,y} = \varphi_{x,y} + 2\pi k \qquad (3.5)$$

where k is an integer, $x = 0, 1, ..., X - 1$ and $y = 0, 1, ..., Y - 1$ and they denote the row and the column of a pixel in the interferogram.

If $| \varphi_{x,y} - \varphi_{x+1,y} |$ is more than π, it corresponds to a column discontinuity [6]. If $| \varphi_{x,y} - \varphi_{x,y+1} |$ is more than π, it corresponds to a row discontinuity [6]. The input of the method is "interferometric phases", which is an X-by-Y matrix. The phase unwrapping algorithm can be summarized as:

- Solution starts by finding the column discontinuities and row discontinuities between the pixels in the radar interferometry. An $(X - 1)$-by-Y matrix is formed to identify the column discontinuities and an X-by-$(Y - 1)$ matrix is formed to identify the row discontinuities. Entries in the discontinuity matrixes get $0, 1$ or -1. If there is no discontinuity between two neighboring pixels, the value of the entry is equal to 0. If there is a discontinuity between two neighboring pixels, the value of the entry is equal to 1 or -1. (the sign shows the small pixel value in the discontinuity pair.)

- Then total number of all of the column and row discontinuities is calculated as the discontinuity sum.

- 2π is added to the small pixel values in all of the discontinuity pairs and then the new discontinuity matrixes are formed between "new interferometric phases" and the new discontinuity sum is found. If the discontinuity sum does not increase, "interferometric phases" are updated with "new interferometric phases".

- The next search starts with the updated interferometric phase values. The above operations are applied to the updated interferometric phases.

- The same process is repeated until the discontinuity sum becomes zero and the final interferometric phase image becomes the output.
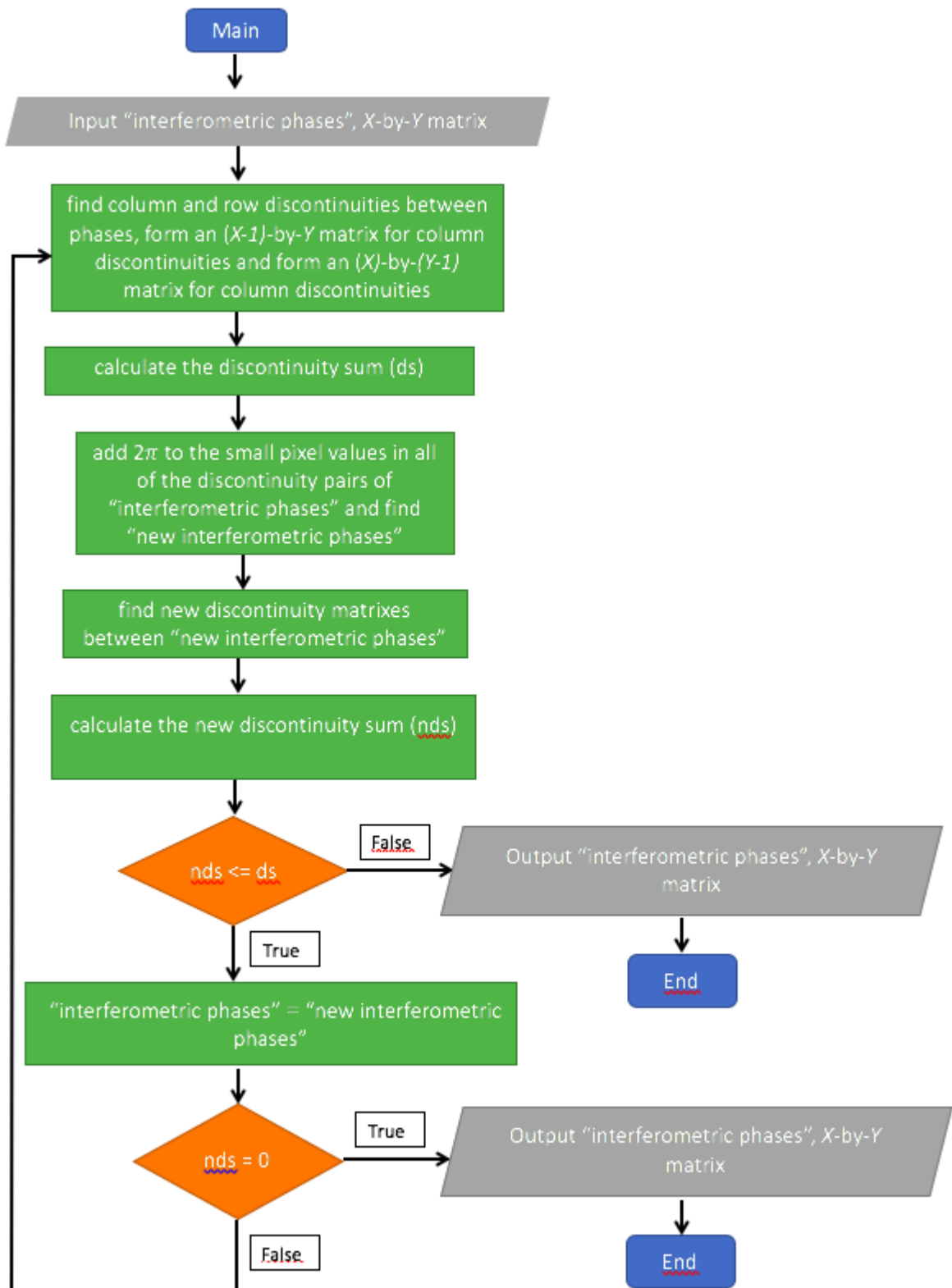
Figure 3.2. Flowchart of the 2D phase unwrapping algorithm.

In Table 3.1, initial phase values of the pixels in the interferogram are given as an example and the discontinuity matrices are given in Table 3.2 and 3.3. The discontinuity sum can be found by summing the absolute value of all of the entries in both column and row discontinuity matrices and the discontinuity sum is 9 in the given interferometric phase image.

Table 3.1. Initial values of the pixels in the interferometric phase image (4-by-7 matrix), unit is radian.

1.7	-3.0	-1.7	-0.3	1.0	2.6	-2.1
1.8	-3.1	-1.7	-0.3	0.9	2.4	-2.4
1.9	3.1	-1.7	-0.4	1.0	2.3	-2.2
2.0	3.0	-1.8	-0.5	1.3	2.3	-1.9

Table 3.2. Column discontinuity matrix (3-by-7 matrix).

0	0	0	0	0	0	0
0	1	0	0	0	0	0
0	0	0	0	0	0	0

Table 3.3. Row discontinuity matrix (4-by-6 matrix).

1	0	0	0	0	1
1	0	0	0	0	1
0	1	0	0	0	1
0	1	0	0	0	1

Then 2π is added to the small pixel values in all of the discontinuity pairs and the discontinuity sum is reduced to 5, so the interferometric phase values are updated. In

Table 3.4, updated phase values of the pixels in the interferogram is given and the new discontinuity matrices are given in Table 3.5 and 3.6. Then the algorithm iterates the procedure over the updated interferometric phases and the next search starts. Then 2π is added to the small pixel values in all of the discontinuity pairs and updated phase values of the pixels in the interferogram is given in Table 3.7.

Table 3.4. Phase values of the pixels in the interferogram (4-by-7 matrix) after the first search, unit is radian.

1.7	3.2	-1.7	-0.3	1.0	2.6	4.1
1.8	3.1	-1.7	-0.3	0.9	2.4	3.8
1.9	3.1	4.5	-0.4	1.0	2.3	4.0
2.0	3.0	4.4	-0.5	1.3	2.3	4.3

Table 3.5. Column discontinuity matrix (3-by-7 matrix) after the first search.

0	0	0	0	0	0	0
0	0	1	0	0	0	0
0	0	0	0	0	0	0

Table 3.6. Row discontinuity matrix (4-by-6 matrix) after the first search.

0	1	0	0	0	0
0	1	0	0	0	0
0	0	1	0	0	0
0	0	1	0	0	0

Table 3.7. Phase values of the pixels in the interferogram (4-by-7 matrix) after the second search, unit is radian.

1.7	3.2	4.5	-0.3	1.0	2.6	4.1
1.8	3.1	4.5	-0.3	0.9	2.4	3.8
1.9	3.1	4.5	5.8	1.0	2.3	4.0
2.0	3.0	4.4	5.7	1.3	2.3	4.3

In Table 3.8, final phase values of the pixels in the interferogram can be seen. The phase unwrapping algorithm terminates when all of the discontinuities are removed. After the last search is over, the discontinuity sum is 0. If the initial and final values of the pixels in the interferometric phase image are compared, it can be seen that 2π is added to the initial pixel values in 2nd column, 3rd column, 4th column, 5th column, 6th column and 4π is added to the initial pixel values in the last column.

Table 3.8. Final values of the pixels in the interferometric phase image (4-by-7 matrix) after phase unwrapping, unit is radian.

1.7	3.2	4.5	5.9	7.2	8.8	10.4
1.8	3.1	4.5	5.9	7.1	8.6	10.2
1.9	3.1	4.5	5.8	7.2	8.5	10.3
2.0	3.0	4.4	5.7	7.5	8.5	10.7

After phase unwrapping algorithm is applied, the interferometric phases can be translated into the displacements to detect changes and receive the velocity field by using equation 3.2 or equation 3.4.
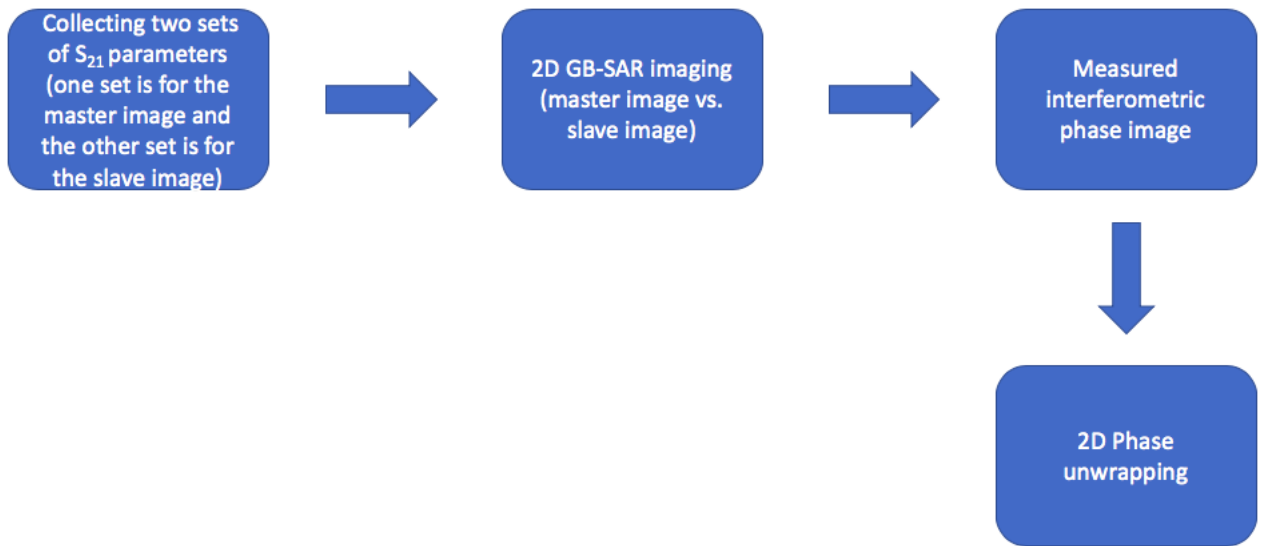
Figure 3.3. Block diagram for 2D phase unwrapping.

3.2. Atmospheric and Instrumental Correction on GB-SAR Interferometry

GB-SAR interferometry is a successful estimate of the displacement of the objects in two SAR images only if coherence or correlation between two SAR images is high [4]. Main sources of small coherence are thermal noise, instrumental noise and atmospheric delay [25]. Also, rainy weather is one of the powerful decorrelation sources, it should be considered in the planning process and dry weather should be preferred for making GB-SAR measurements. Thermal noise is related to SNR, so it can be neglected [25].

The objective of analyzing atmospheric and instrumental decorrelation sources is to determine the true phase changes and the actual displacements. Steady and stable objects with high reflectivity are used or placed as reference during the measurements to correct the atmospheric delay and the instrumental instability with an emprical approach [25].

3.2.1. Instrumental Instability

Δr is the true displacement and it is translated into the true interferometric phase φ by means of the relationship,

$$\varphi = \frac{4\pi f_c \Delta r}{c} \tag{3.6}$$

Δr is equal to $(r_2 - r_1)$,

$$\varphi = \frac{4\pi f_c r_2}{c} - \frac{4\pi f_c r_1}{c} \tag{3.7}$$

The temporal instability of the frequency of VNA affects the interferometric phase in the measurements. ϵ_f is the possible drift of the centre frequency between two SAR images and it is accepted that the frequency drift occurs at the second measurement.

$$\varphi' = \frac{4\pi (f_c + \epsilon_f) r_2}{c} - \frac{4\pi f_c r_1}{c} \tag{3.8}$$

where φ' is the measured interferometric phase.

$$\varphi' = \frac{4\pi f_c \Delta r'}{c} \tag{3.9}$$

where $\Delta r'$ is the displacement from the measured phase. Since $r_2 \approx r_1 = R$,

$$\Delta r' = \Delta r + \frac{\epsilon_f R}{f_c} \tag{3.10}$$

ϵ_f / f_c is accepted as α_f and equation 3.10 becomes,

$$\Delta r' = \Delta r + \alpha_f R \tag{3.11}$$

If the above equation is checked, it can be easily seen that the effect of the frequency drift is range dependent. Then it is supposed that there is no frequency drift of the centre frequency between two SAR images, but the phases might be measured with an offset $\delta\varphi$ because of a systematic error.

$$\Delta r' = \frac{\lambda_c}{4\pi}(\varphi + \delta\varphi) \tag{3.12}$$

Since the true displacement Δr is equal to $(\lambda_c\varphi)/(4\pi)$, equation 3.12 is converted into equation 3.13,

$$\Delta r' = \Delta r + \frac{\lambda_c \delta\varphi}{4\pi} \tag{3.13}$$

$(\lambda_c\delta\varphi)/(4\pi)$ is accepted as β_φ and equation 3.13 becomes,

$$\Delta r' = \Delta r + \beta_\varphi \tag{3.14}$$

The above equation shows the fact that the possible phase offset is range independent. After two contributions are taken into consideration to terminate the effect of the instability of the phase and the frequency of the transceiver,

$$\Delta r' = \Delta r + \alpha_f R + \beta_\varphi \tag{3.15}$$

3.2.2. Atmospheric Delay

Atmospheric state strongly affects SAR measurements and interferometric phases. The speed of the radar wave depends on atmospheric refractivity n_{atm} and atmospheric refractivity depends on air humidity, temperature and air pressure, and

$$\varphi = \frac{4\pi\Delta r}{\lambda_c} \tag{3.16}$$

Δr is equal to $(r_2 - r_1)$,

$$\varphi = \frac{4\pi r_2}{\lambda_c} - \frac{4\pi r_1}{\lambda_c} \tag{3.17}$$

ϵ_{atm} is the drift in atmospheric refractivity and equation 3.17 is converted into,

$$\varphi' = \frac{4\pi(1 + \epsilon_{atm})r_2}{\lambda_c} - \frac{4\pi r_1}{\lambda_c} \tag{3.18}$$

Since $r_2 \approx r_1 = R$,

$$\Delta r' = \Delta r + \epsilon_{atm}R \tag{3.19}$$

If the above equation is checked, it is obvious that the effect of the atmospheric delay is range dependent. After the effects of both the instrumental instability and the atmospheric delay are taken into consideration,

$$\Delta r' = \Delta r + (\alpha_f + \epsilon_{atm})R + \beta_\varphi \tag{3.20}$$

Then the final equation for the true displacement becomes,

$$\Delta r = \Delta r' - (\alpha_f + \epsilon_{atm})R - \beta_\varphi \tag{3.21}$$

Since the steady and stable objects are chosen as reference, their true displacements are equal to zero.

$$\Delta r' - (\alpha_f + \epsilon_{atm})R + \beta_\varphi = 0 \tag{3.22}$$

The above equation gives that two steady objects which are at different ranges should be chosen for atmospheric and instrumental correction. After $(\alpha_f + \epsilon_{atm})$ and

β_φ are found, the measured interferometric phase at the bth pixel of the radar interferometry is translated into the true displacement Δr_m in the mth pixel by means of the relationship,

$$\Delta r_m = \frac{\lambda_c}{4\pi}\varphi_m - (\alpha_f + \epsilon_{atm})R_m - \beta_\varphi \tag{3.23}$$

where R_m is the range of the mth pixel of the radar interferometry.
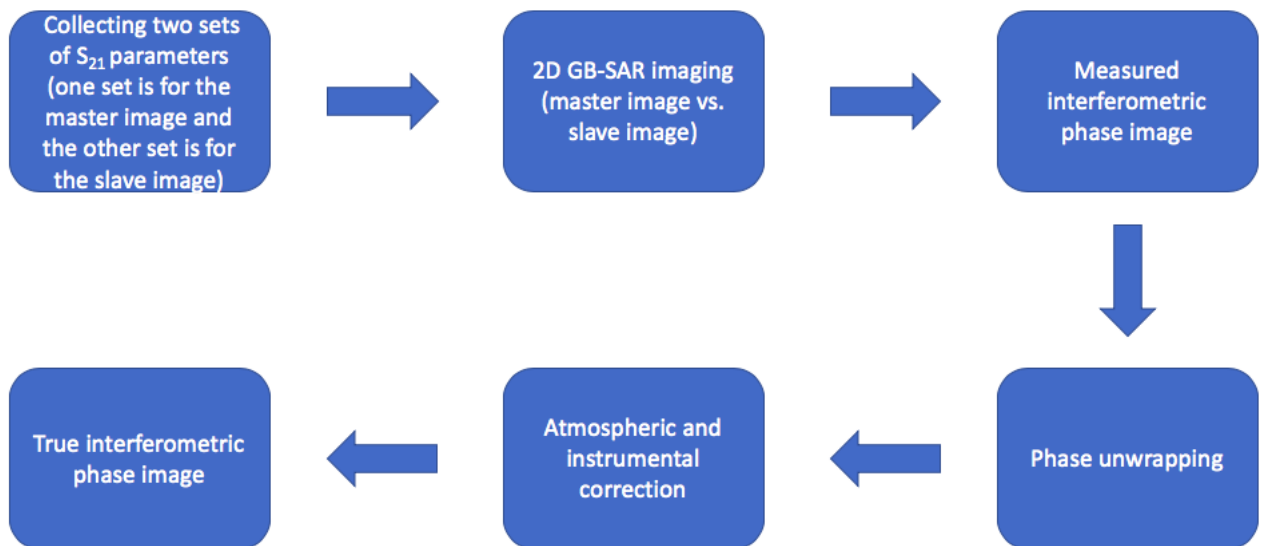
Figure 3.4. Block diagram for atmospheric and instrumental correction.

4. 2D RADAR IMAGES AND INTERFEROMETRIC RESULTS

Two trihedral corner reflectors are placed across the GB-SAR system for indoor experimental setup. Indoor measurements are made in a conference room of Boğaziçi University, Electrical-Electronics Engineering Department. VNA and antennas are calibrated in 201 steps from 5 GHz to 6 GHz for most of indoor measurements and they are calibrated in 201 steps from 4 GHz to 5 GHz for other indoor measurements. The pixel sizes are selected as $5cm \times 5cm$ for most of GB-SAR radar images and the pixel sizes are selected as $2cm \times 2cm$ for other 2D GB-SAR images. The target region for radar images is determined as $4m \times 4m$ for most of indoor measurements and the target region for radar images is determined as $4m \times 5m$ for other indoor measurements. Also, a metallic pipe is located onto the reflector to apply phase unwrapping algorithm in the last indoor measurement.

Table 4.1. Radar parameters of the calibration from 5 GHz to 6 GHz.

Parameter (unit)	Symbol	Value
Bandwith (GHz)	B	1
Frequency step (MHz)	Δf	5
Centre frequency (GHz)	f_c	5.5
Centre wavelength (m)	λ_c	0.0545
Displacement for unit interferometric phase (m)	$\frac{\lambda_c}{4\pi}$	0.0043
Maximum displacement in modulo 2π (m)	$\frac{\lambda_c}{4\pi}\pi$	0.0136
Aperture length (m)	L	2
Azimuth point numbers	N	101
Range resolution (m)	$\Delta R = \frac{c}{2B}$	0.15
Azimuth resolution (m)	$\Delta \vartheta = \frac{\lambda_c}{2L}R$	0.1363 @ 10
Non ambigous range (m)	$R_{na} = \frac{c}{2\Delta f}$	0.3

Table 4.2. Radar parameters of the calibration from 4 GHz to 5 GHz.

Parameter (unit)	Symbol	Value
Bandwith (GHz)	B	1
Frequency step (MHz)	Δf	5
Centre frequency (GHz)	f_c	4.5
Centre wavelength (m)	λ_c	0.0666
Displacement for unit interferometric phase (m)	$\frac{\lambda_c}{4\pi}$	0.0053
Maximum displacement in modulo 2π (m)	$\frac{\lambda_c}{4\pi}\pi$	0.0167
Aperture length (m)	L	2
Azimuth point numbers	N	101
Range resolution (m)	$\Delta R = \frac{c}{2B}$	0.15
Azimuth resolution (m)	$\Delta \vartheta = \frac{\lambda_c}{2L}R$	0.1666 @ 10
Non ambigous range (m)	$R_{na} = \frac{c}{2\Delta f}$	0.3

Two trihedral corner reflectors or two blocks of stones are placed across the GB-SAR system for outdoor experimental setups. VNA and antennas are calibrated in 201 steps from 5 GHz to 6 GHz for outdoor measurements. The pixel sizes of GB-SAR images are selected as $5cm \times 5cm$. The target region for radar images is determined as $4m \times 4m$. As mentioned before, the center of the rail is accepted as the origin, $(0,0)$, in all of indoor and outdoor radar images.

After S_{21} parameters of the environment are collected, one of the objects is moved, S_{21} parameters of the environment are collected again, master and slave radar images are formed and then GB-SAR interferometry is found. Also, one of the objects is kept steady in the measurements because the steady object is used as reference for atmospheric and instrumental correction. This work is done in close range, so it is not needed to calculate the range-dependent variables, $(\alpha_f + \epsilon_{atm})$ for atmospheric delay and instrumental instability and one steady object is enough to calculate the range independent variable, β_φ.

Two different methods, which are explained in chapter 2, are used to form 2D radar images. In all of the GB-SAR images, the pixels having a signal 40 dB below

the maximum amplitude are masked out and the scatter characteristics of these pixels are equalized to zero to get rid of noise-corrupted areas because there is no useful information in these areas [26]. The radar images which are obtained by delay-and-sum method are used in GB-SAR interferometry because delay-and-sum algorithm is more robust and have less computational burden. The interferometric phases are translated into the displacements by using equation 3.2 or equation 3.4.

4.1. Outdoor Measurement-1

Two corner reflectors are located across the GB-SAR system for the first outdoor measurement. The location of the one of the reflectors is $(-1, 2.5)$ and the location of the other reflector is $(0.25, 4)$. The schematic for outdoor measurement-1 is given in Figure 4.2. Two reflectors at given locations can be easily seen in the radar images, Figure 4.3 and 4.4.

Figure 4.1. Setup for outdoor measurement-1.

Figure 4.2. Schematic for outdoor measurement-1.

Figure 4.3. Outdoor measurement-1, the pixel sizes are $5cm \times 5cm$, calibration is from 5 GHz to 6 GHz.

Figure 4.4. Outdoor measurement-1, delay-and-sum algorithm, the pixel sizes are $5cm \times 5cm$, calibration is from 5 GHz to 6 GHz.

4.2. Outdoor Measurement-2

Two blocks of stones are located across the GB-SAR system for the second out-door measurements. The location of the one of the blocks is $(-1, 5)$ and the location of the other block is $(0.5, 5)$. The schematic for outdoor measurement-2 is given in Figure 4.6. Two blocks at given locations can be easily seen in the radar images, Figure 4.7 and 4.8.

Figure 4.5. Outdoor measurement setup-2.

Figure 4.6. Schematic for outdoor measurement-2.

Figure 4.7. Outdoor measurement-2, the pixel sizes are $5cm \times 5cm$, calibration is from 5 GHz to 6 GHz.

Figure 4.8. Outdoor measurement-2, delay-and-sum algorithm, the pixel sizes are $5cm \times 5cm$, calibration is from 5 GHz to 6 GHz.

4.2.1. Radar Interferometry-1

The block of stones whose coordinates are $(0.5, 5)$ is moved 7 mm towards the GB-SAR system in the range direction and the other block is kept steady. The schematic for the first interferometry measurements is given in Figure 4.9. VNA and antennas are calibrated in 201 steps from 5 GHz to 6 GHz. Then results of interferometric phase values and displacements are received in Table 4.3, 4.4, and 4.5. There are displacements less than quarter of 1 mm in the pixels of the steady stones and there are displacements around 7 mm in the pixels of moving stones. Results are parallel with experimental setup as expected.
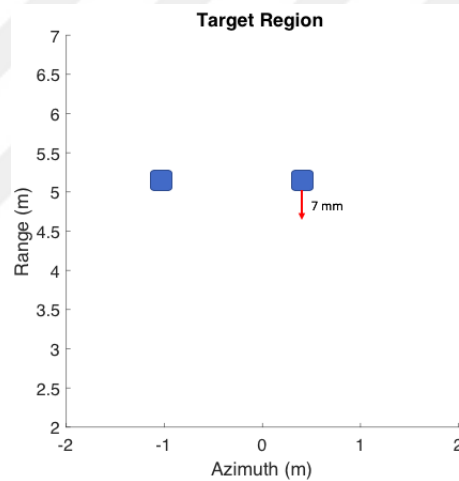
Figure 4.9. Schematic for radar interferometry-1, outdoor measurement-2.
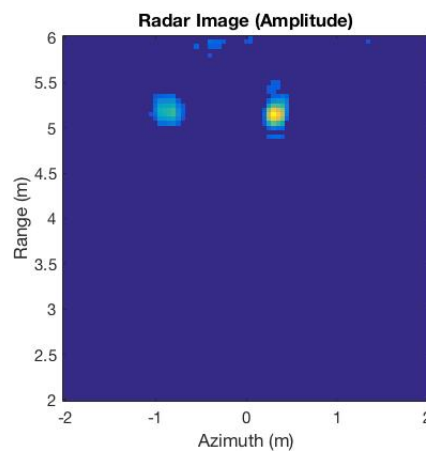
Figure 4.10. Master image-1 (outdoor measurement-2), delay-and-sum algorithm, the pixel sizes are $5cm \times 5cm$, calibration is from 5 GHz to 6 GHz.
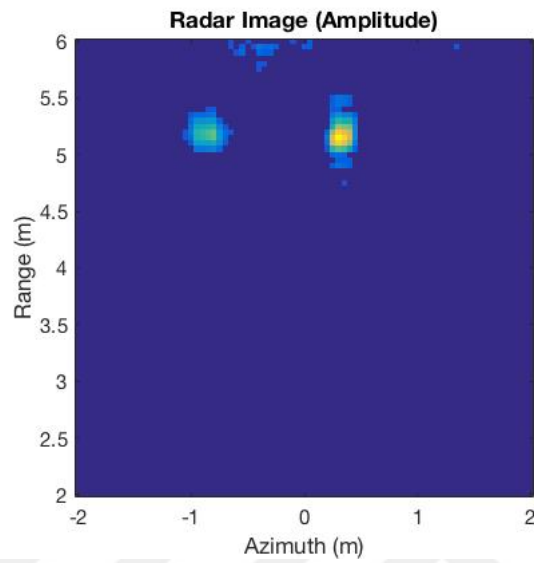
Figure 4.11. Slave image-1 (outdoor measurement-2), delay-and-sum algorithm, the pixel sizes are $5cm \times 5cm$, calibration is from 5 GHz to 6 GHz.
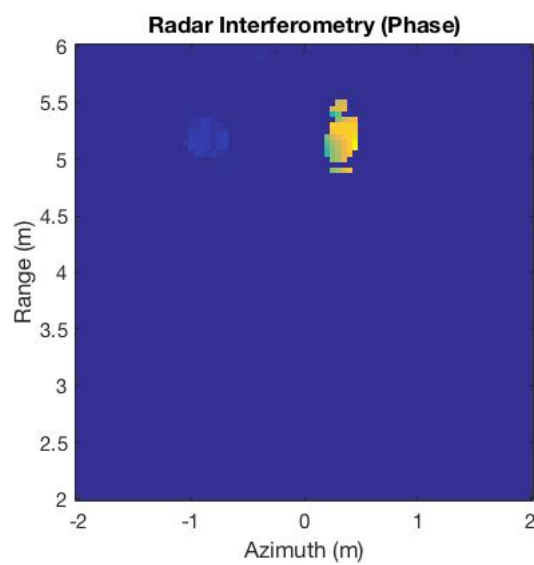
Figure 4.12. Interferometric phases-1 (outdoor measurement-2).

Table 4.3. Interferometric phase values of the pixels of the steady stones, unit is radian (radar interferometry-1, outdoor measurement-2).

0	0.0590	0.0714	0.0441	0.0794	0.0377
0.0939	0.0629	0.0592	0.0658	0.0575	0.0671
0.0789	0.0632	0.0589	0.0697	0.0550	0.0682
0.0756	0.0610	0.0627	0.0696	0.0560	0.0626
0.0681	0.0585	0.0653	0.0710	0.0540	0.0601
0.0538	0.0543	0.0662	0.0701	0.0478	0.0582
0.0408	0.0480	0.0620	0.0605	0.0400	0

Table 4.4. Interferometric phase values of the pixels of moving stones, unit is radian (radar interferometry-1, outdoor measurement-2).

0.9595	1.2259	1.3875	1.5578	1.7113	0
1.0384	1.2494	1.4136	1.5716	1.7307	2.0013
1.1035	1.3069	1.4728	1.6139	1.7482	1.9495
1.2049	1.4328	1.5894	1.6902	1.7793	1.8691
0	1.6759	1.7529	1.7745	1.8029	1.8025
0	1.7953	1.7398	1.7509	1.7596	1.7369
0	0	1.2377	1.4753	1.6006	1.6152

Table 4.5. The displacements in the pixels of moving stones, unit is mm (radar interferometry-1, outdoor measurement-2).

4.1620	5.3176	6.0186	6.7573	7.4231	0
4.5043	5.4195	6.1318	6.8171	7.5072	8.6810
4.7866	5.6689	6.3886	7.0006	7.5832	8.4563
5.2265	6.2151	6.8943	7.3316	7.7181	8.1076
0	7.2695	7.6035	7.6972	7.8204	7.8187
0	7.7875	7.5467	7.5949	7.6326	7.5341
0	0	5.3688	6.3994	6.9429	7.0062

4.3. Indoor Measurement-1

Two corner reflectors are located across the GB-SAR system for the first indoor measurements. The location of the one of the reflectors is $(-0.5, 6.5)$ and the location of the other reflector is $(1, 5.25)$. The schematic for indoor measurement-1 is given in Figure 4.14. Two reflectors at given locations can be easily seen in the radar images, Figure 4.15 and 4.16.

Figure 4.13. Indoor measurement setup-1.
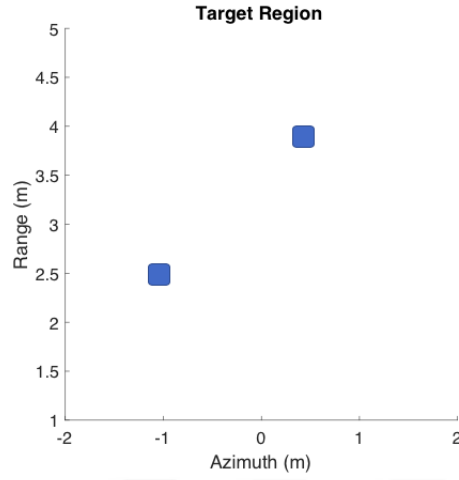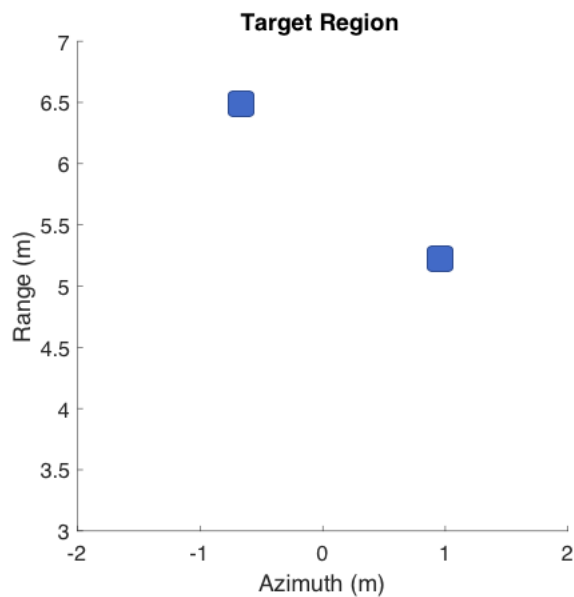

Figure 4.14. Schematic for indoor measurement-1.
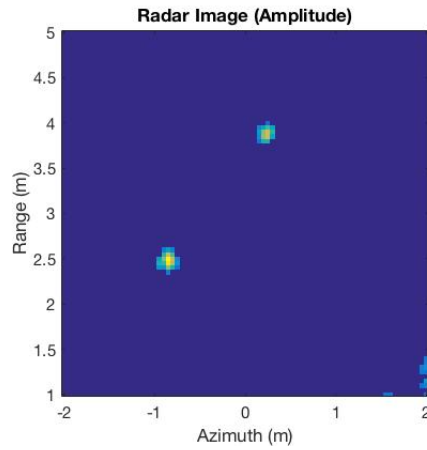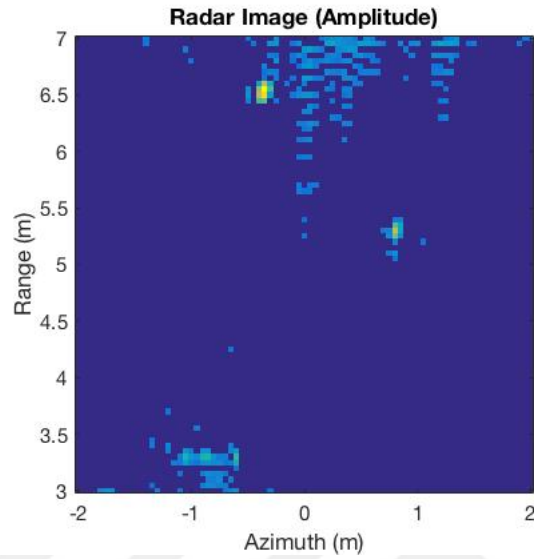
Figure 4.15. Indoor measurement-1, the pixel sizes are $5cm \times 5cm$, calibration is from 5 GHz to 6 GHz.

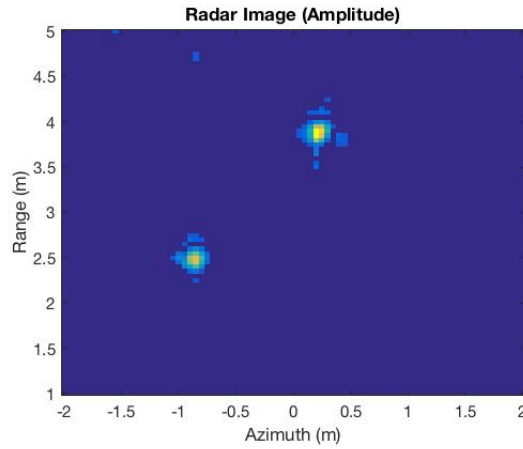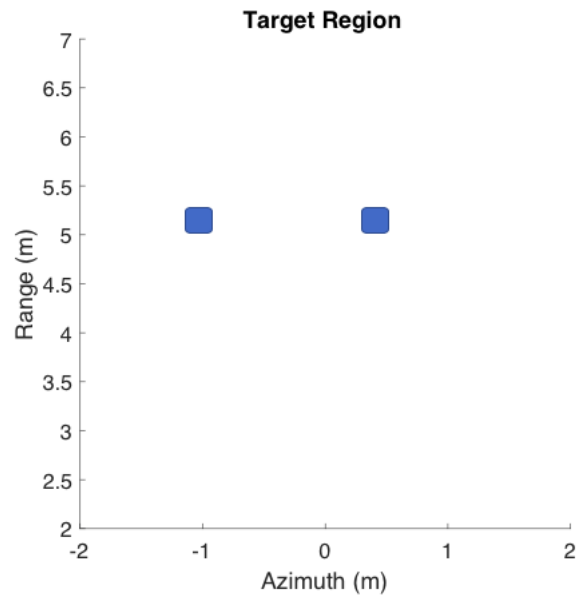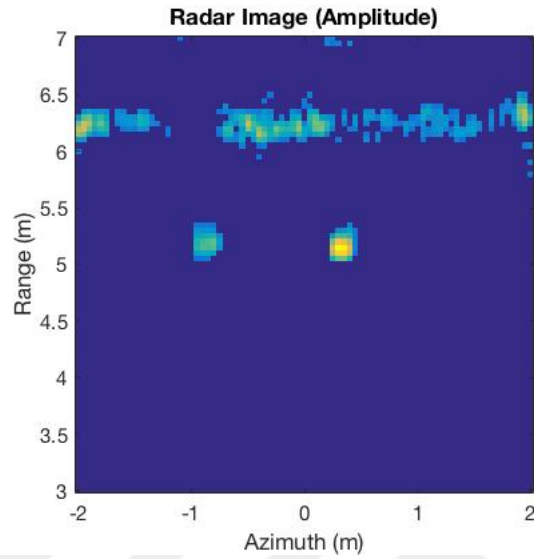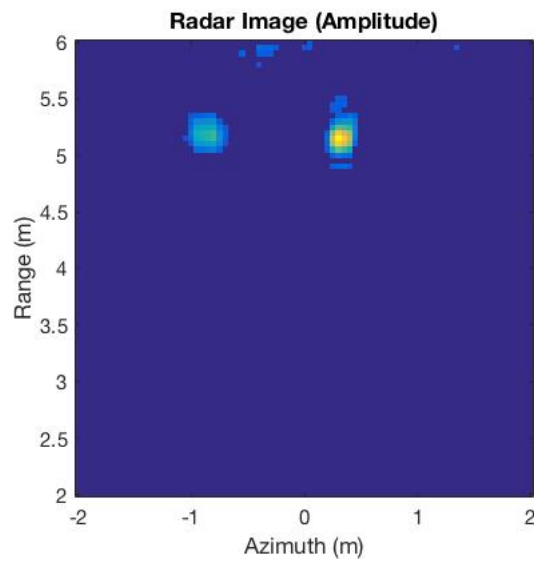
Figure 4.16. Indoor measurement-1, delay-and-sum algorithm, the pixel sizes are $5cm \times 5cm$, calibration is from 5 GHz to 6 GHz.

4.3.1. Radar Interferometry-1

The reflector whose coordinates are $(-0.5, 6.5)$ is moved 1 cm towards the GB-SAR system in the range direction and the other reflector is kept steady. The schematic for the first interferometry measurements is given in Figure 4.17. VNA and antennas are calibrated in 201 steps from 5 GHz to 6 GHz. Then results of interferometric phase values and displacements are received in Table 4.6, 4.7 and 4.8. There are displacements less than quarter of 1 mm in the pixels of the steady reflector and there are displacements around 1 cm in the pixels of moving reflector. Results are parallel with experimental setup as expected.

Figure 4.17. Schematic for radar interferometry-1, indoor measurement-1.

Figure 4.18. Master image-1 (indoor measurement-1), delay-and-sum algorithm, the pixel sizes are $5cm \times 5cm$, calibration is from 5 GHz to 6 GHz.

Figure 4.19. Slave image-1 (indoor measurement-1), delay-and-sum algorithm, the pixel sizes are $5cm \times 5cm$, calibration is from 5 GHz to 6 GHz.

Figure 4.20. Interferometric phases-1 (indoor measurement-1).

Table 4.6. Interferometric phase values of the pixels of the steady reflector (radar interferometry-1, indoor measurement-1).

0	0	0.0007	0.0011	0.0007	0
0	0	0.0065	0.0008	0	0
0	0	0.0060	0.0027	0.0226	0
0	0.0068	0.0022	0.0072	0.0099	0
0	0.0358	0.0065	0.0114	0.0023	0
0	0.0710	0	0.0173	0.0026	0

Table 4.7. Interferometric phase values of the pixels of moving reflector (radar interferometry-1, indoor measurement-1).

0	0	1.9681	1.9011	0	0
2.4506	0	2.2836	2.3306	2.3566	0
2.4009	0	2.3534	2.3759	2.3973	2.2676
2.3365	0	2.3586	2.3879	2.4218	2.2470
2.2997	1.9921	2.3508	2.3967	2.4271	0
0	0	2.3428	2.4024	2.3089	0

Table 4.8. The displacements in the pixels of moving reflector, unit is cm (radar interferometry-1, indoor measurement-1).

0	0	0.8537	0.8246	0	0
1.0630	0	0.9906	1.0109	1.0222	0
1.0414	0	1.0208	1.0306	1.0399	0.9836
1.0135	0	1.0231	1.0358	1.0505	0.9747
0.9975	0.8641	1.0197	1.0396	1.0528	0
0	0	1.0162	1.0421	1.0015	0

4.3.2. Radar Interferometry-2

The reflector whose coordinates are $(-0.5, 6.5)$ is moved 1 cm towards the GB-SAR system in the range direction and the other reflector is kept steady. The schematic

for the second interferometry measurements is given in Figure 4.21. VNA and antennas are calibrated in 201 steps from 4 GHz to 5 GHz. Then results of interferometric phase values and displacements are received in Table 4.9 and 4.10. There are displacements around 1 cm in the pixels of moving reflector. Results are parallel with experimental setup as expected although a different calibration interval (instead of 5 GHz - 6 GHz) is used in radar interferometry-2.

Figure 4.21. Schematic for radar interferometry-2, indoor measurement-1.

Figure 4.22. Master image-2 (indoor measurement-1), delay-and-sum algorithm, the pixel sizes are $5cm \times 5cm$, calibration is from 4 GHz to 5 GHz.

Figure 4.23. Slave image-2 (indoor measurement-1), delay-and-sum algorithm, the pixel sizes are $5cm \times 5cm$, calibration is from 4 GHz to 5 GHz.

Figure 4.24. Interferometric phases-2 (indoor measurement-1).

Table 4.9. Interferometric phase values of the pixels of moving reflector (radar interferometry-2, indoor measurement-1).

1.8254	0	0	1.9007	2.0500	0
1.8131	1.5828	2.2400	2.0112	1.9394	1.8063
1.7608	1.6346	2.2315	2.0025	1.9386	1.8506
1.8145	1.7762	2.1141	1.9805	1.9461	1.9006
1.9587	2.0901	1.9799	1.9560	1.9627	1.9685
0	0	1.8326	1.9161	1.9903	2.0673

Table 4.10. The displacements in the pixels of moving reflector, unit is cm (radar interferometry-2, indoor measurement-1).

0.9678	0	0	1.0077	1.0868	0
0.9612	0.8391	1.1876	1.0663	1.0282	0.9576
0.9335	0.8666	1.1831	1.0617	1.0278	0.9811
0.9620	0.9417	1.1208	1.0500	1.0317	1.0076
1.0384	1.1081	1.0497	1.0370	1.0406	1.0436
0	0	0.9716	1.0158	1.0552	1.0960

4.3.3. Radar Interferometry-3

The reflector whose coordinates are $(-0.5, 6.5)$ is moved 1.5 cm towards the GB-SAR system in the range direction and the other reflector is kept steady. The schematic for the third interferometry measurements is given in Figure 4.25. VNA and antennas are calibrated in 201 steps from 4 GHz to 5 GHz. Then results of interferometric phase values and displacements are received in Table 4.11 and 4.12. There are displacements around 1.5 cm in the pixels of moving reflector. Results are parallel with experimental setup as expected. If the calibration was from 5 GHz to 6 GHz in radar interferometry-3, the interferometric results would not be correct (the displacements would be calculated around 1.22 cm in the opposite direction.) since the maximum displacement is 1.36 cm for this calibration range.
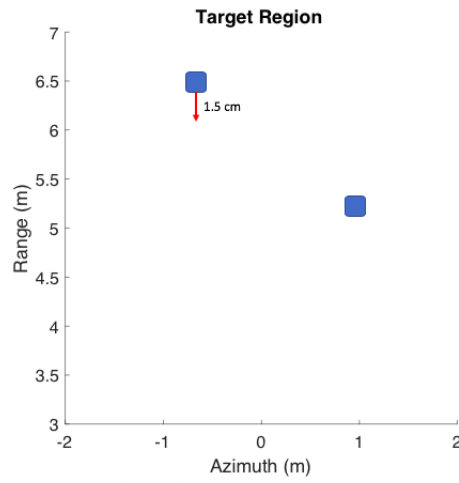
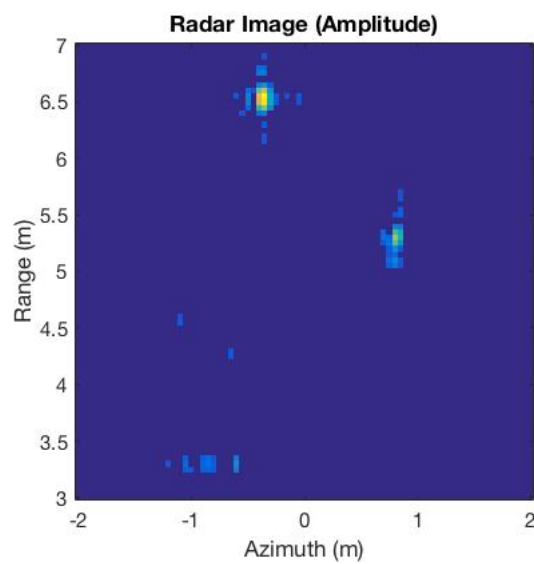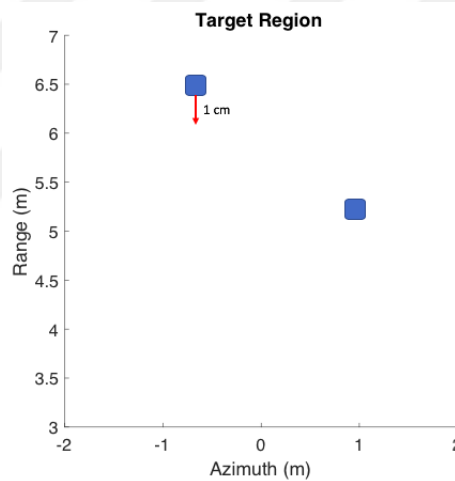Figure 4.25. Schematic for radar interferometry-3, indoor measurement-1.
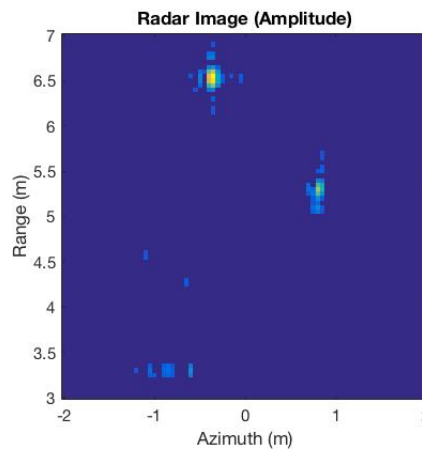

Figure 4.26. Master image-3 (indoor measurement-1), delay-and-sum algorithm, the pixel sizes are $5cm \times 5cm$, calibration is from 4 GHz to 5 GHz.
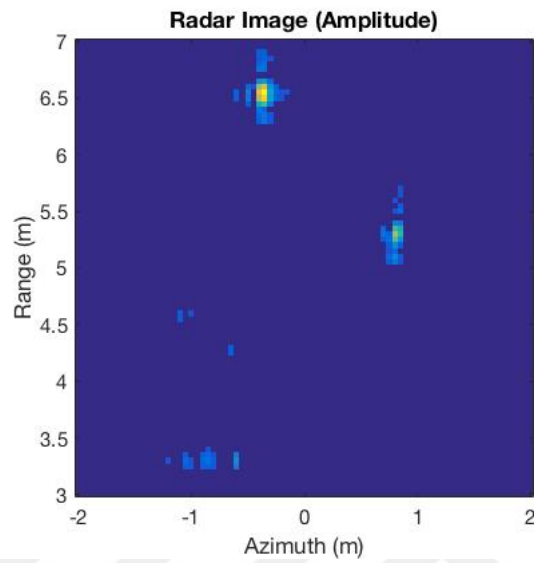

Figure 4.27. Slave image-3 (indoor measurement-1), delay-and-sum algorithm, the pixel sizes are $5cm \times 5cm$, calibration is from 4 GHz to 5 GHz.
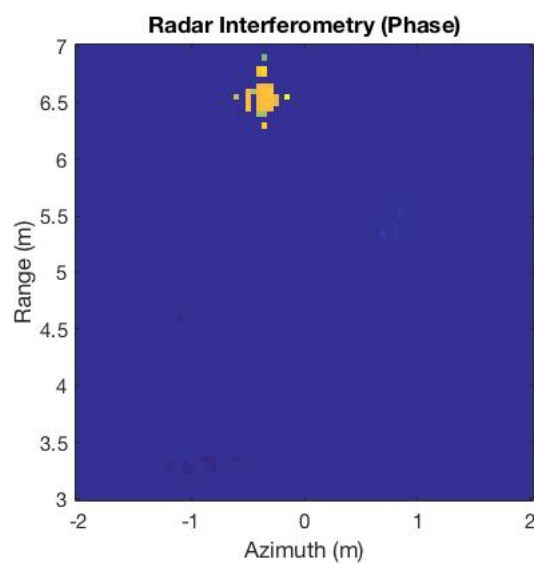
Figure 4.28. Interferometric phases-3 (indoor measurement-1).

Table 4.11. Interferometric phase values of the pixels of moving reflector (radar interferometry-3, indoor measurement-1).

2.6784	0	0	2.8540	0	0
2.6018	2.3852	3.0419	2.9557	2.9043	2.7264
2.5636	2.4526	3.1302	2.9713	2.9144	2.8030
2.6784	2.6442	3.0929	2.9735	2.9409	2.8830
2.8818	3.0479	3.0300	2.9762	2.9804	2.9808
0	0	2.9584	2.9734	3.0370	3.1060

Table 4.12. The displacements in the pixels of moving reflector, unit is cm (radar interferometry-3, indoor measurement-1).

1.4200	0	0	1.5131	0	0
1.3794	1.2645	1.6127	1.5670	1.5398	1.4454
1.3591	1.3003	1.6595	1.5753	1.5451	1.4860
1.4200	1.4019	1.6397	1.5764	1.5592	1.5285
1.5278	1.6159	1.6064	1.5779	1.5801	1.5803
0	0	1.5684	1.5764	1.6101	1.6467

4.3.4. Radar Interferometry-4

The reflector whose coordinates are $(-0.5, 6.5)$ is moved 5 mm towards the GB-SAR system in the range direction and the other reflector is kept steady. The schematic for the forth interferometry measurements is given in Figure 4.29. The pixel sizes of GB-SAR images are selected as $2cm \times 2cm$ and the target region for radar images is determined as $4m \times 5m$. VNA and antennas are calibrated in 201 steps from 5 GHz to 6 GHz. Then results of interferometric phase values and displacements are received in Table 4.13 and 4.14. There are displacements around 5 mm in the pixels of moving reflector. Results are parallel with experimental setup as expected although a different pixel size $(2cm \times 2cm)$ and target region size $(4m \times 5m)$ are used in radar interferometry-4.
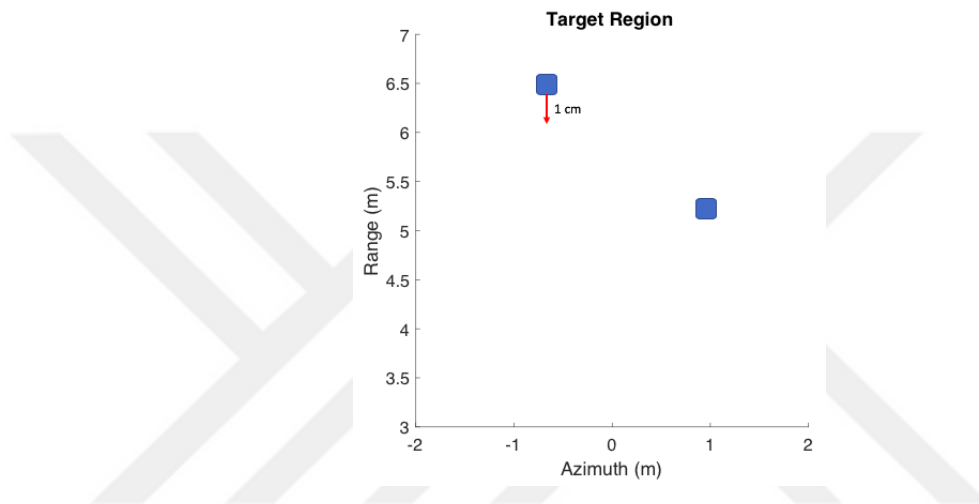

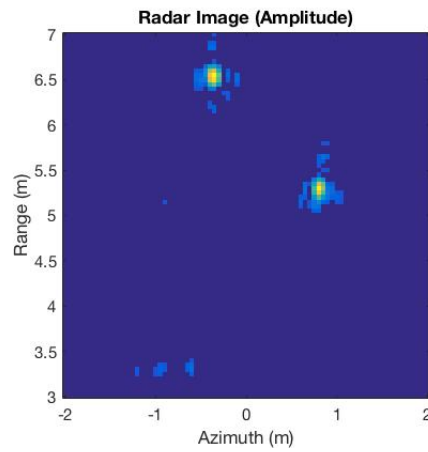Figure 4.29. Schematic for radar interferometry-4, indoor measurement-1.

Figure 4.30. Master image-4 (indoor measurement-1), delay-and-sum algorithm, the pixel sizes are $2cm \times 2cm$, calibration is from 5 GHz to 6 GHz.
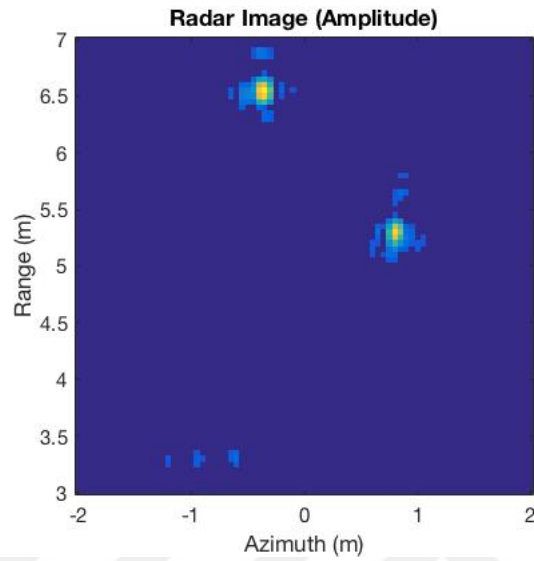

Figure 4.31. Slave image-4 (indoor measurement-1), delay-and-sum algorithm, the pixel sizes are $2cm \times 2cm$, calibration is from 5 GHz to 6 GHz.
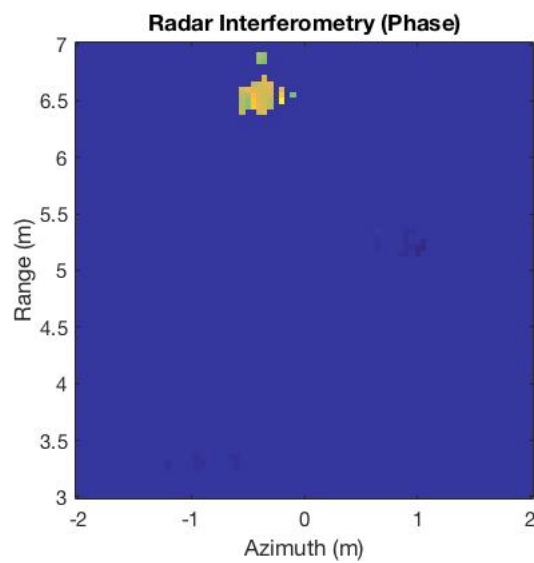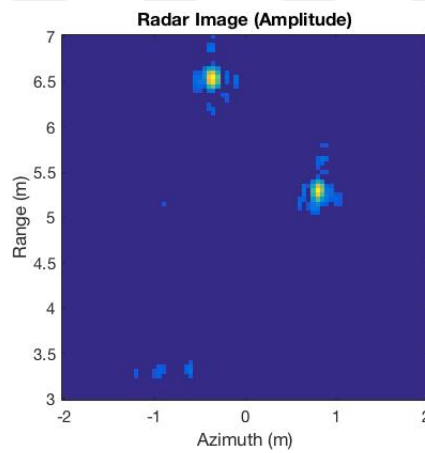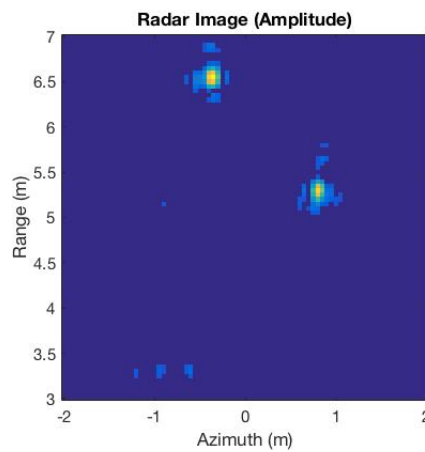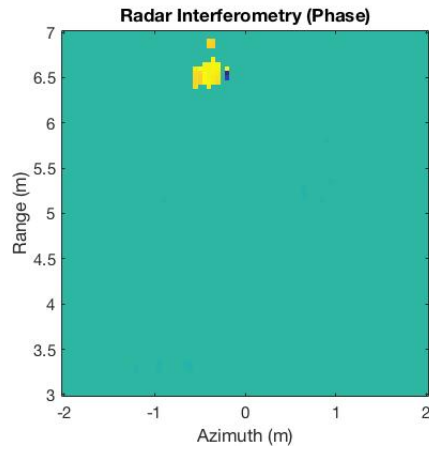

Figure 4.32. Interferometric phases-4 (indoor measurement-1).

Table 4.13. Interferometric phase values of the pixels of moving reflector (radar interferometry-4, indoor measurement-1).

1.2615	1.2524	1.2525	1.2526	1.2521	1.2510	1.2498	1.2508	0
1.2685	1.2568	1.2561	1.2556	1.2549	1.2543	1.2551	1.2613	1.3006
1.2649	1.2580	1.2586	1.2586	1.2584	1.2585	1.2607	1.2705	1.3204
1.2598	1.2586	1.2611	1.2620	1.2623	1.2630	1.2661	1.2780	1.3310
1.2566	1.2596	1.2640	1.2657	1.2664	1.2674	1.2709	1.2833	1.3327
1.2566	1.2617	1.2674	1.2697	1.2705	1.2713	1.2745	1.2859	0
1.2609	1.2650	1.2713	1.2737	1.2741	1.2743	1.2762	1.2852	0
1.2698	1.2691	1.2753	1.2773	1.2768	1.2755	1.2753	1.2805	0
1.2811	1.2720	1.2781	1.2792	1.2770	1.2733	1.2700	1.2717	0

Table 4.14. The displacements in the pixels of moving reflector, unit is mm (radar interferometry-4, indoor measurement-1).

5.4720	5.4325	5.4330	5.4334	5.4312	5.4265	5.4213	5.4256	0
5.5024	5.4516	5.4486	5.4464	5.4434	5.4408	5.4442	5.4711	5.6416
5.4868	5.4568	5.4594	5.4594	5.4586	5.4590	5.4685	5.5110	5.7275
5.4646	5.4594	5.4703	5.4742	5.4755	5.4785	5.4920	5.5436	5.7735
5.4507	5.4638	5.4828	5.4902	5.4933	5.4976	5.5128	5.5666	5.7808
5.4507	5.4729	5.4976	5.5076	5.5110	5.5145	5.5284	5.5778	0
5.4694	5.4872	5.5145	5.5249	5.5267	5.5275	5.5358	5.5748	0
5.5080	5.5050	5.5319	5.5405	5.5384	5.5327	5.5319	5.5544	0
5.5570	5.5175	5.5440	5.5488	5.5392	5.5232	5.5089	5.5162	0

4.4. Indoor Measurement-2

Two corner reflectors are located across the GB-SAR system for the second indoor measurements. The location of the one of the reflectors is $(-1, 3.5)$ and the location of the other reflector is $(1, 4.5)$. The schematic for indoor measurement-2 is given in Figure 4.34. Two reflectors at given locations can be easily seen in the radar images, Figure 4.35 and 4.36. These measurements are made to analyze the interferometric results of horizontal (azimuth direction) and crosswise movements.

Figure 4.33. Indoor measurement setup-2.
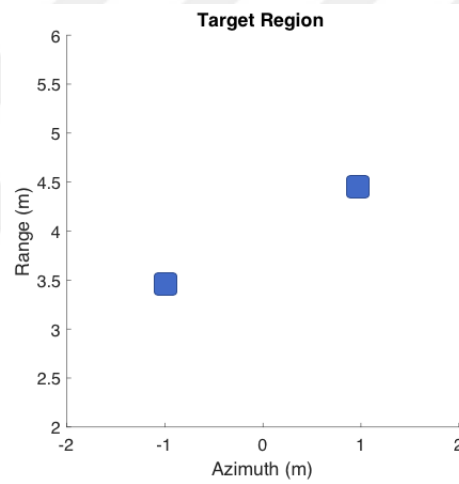
Figure 4.34. Schematic for indoor measurement-2.
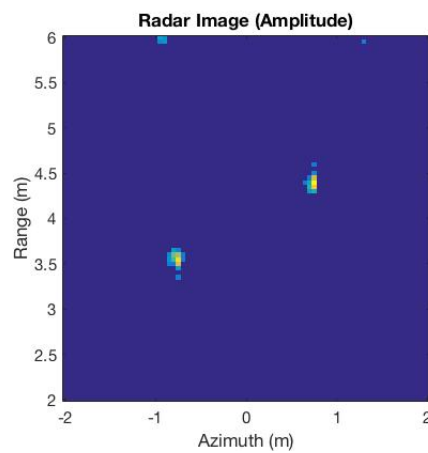
Figure 4.35. Indoor measurement-2, the pixel sizes are $5cm \times 5cm$, calibration is from 5 GHz to 6 GHz.

Figure 4.36. Indoor measurement-2, delay-and-sum algorithm, the pixel sizes are $5cm \times 5cm$, calibration is from 5 GHz to 6 GHz.

4.4.1. Radar Interferometry-1

The reflector whose coordinates are $(-1, 3.5)$ is moved 1 cm to the right in the azimuth direction and the other reflector is kept steady. The schematic for the first interferometry measurements is given in Figure 4.37. VNA and antennas are calibrated in 201 steps from 5 GHz to 6 GHz. Then results of interferometric phase values and displacements are received in Table 4.15 and 4.16. Since the movement in azimuth direction cannot be recognized by GB-SAR interferometry, results are parallel with experimental setup as expected.
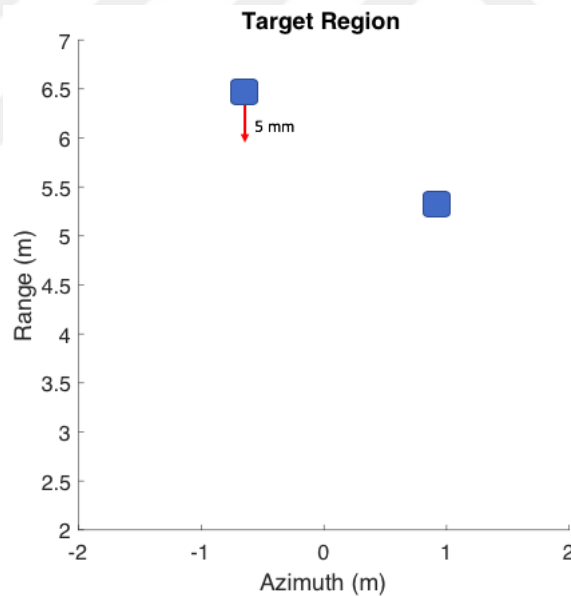
Figure 4.37. Schematic for radar interferometry-1, indoor measurement-2.
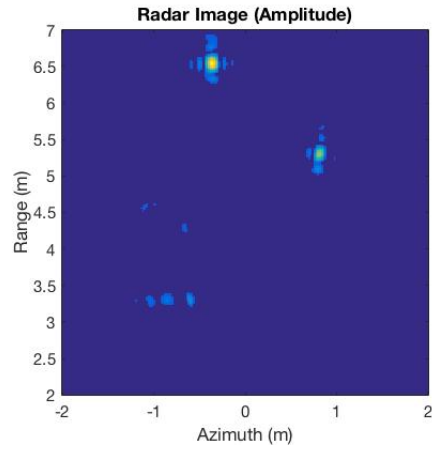

Figure 4.38. Master image-1 (indoor measurement-2), delay-and-sum algorithm, the pixel sizes are $5cm \times 5cm$, calibration is from 5 GHz to 6 GHz.
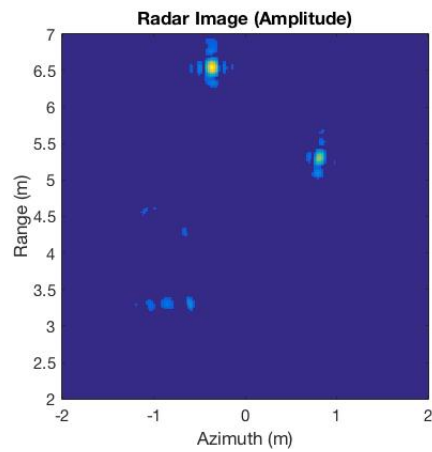

Figure 4.39. Slave image-1 (indoor measurement-2), delay-and-sum algorithm, the pixel sizes are $5cm \times 5cm$, calibration is from 5 GHz to 6 GHz.
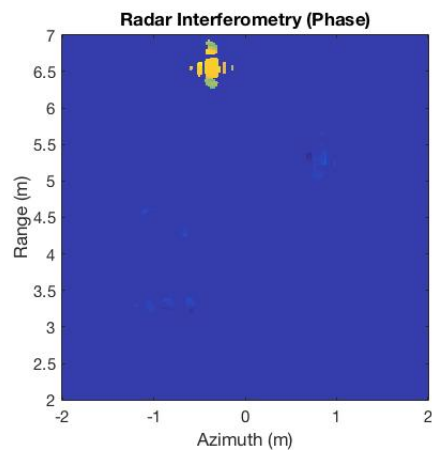
Figure 4.40. Interferometric phases-1 (indoor measurement-2).

Table 4.15. Interferometric phase values of the pixels of moving reflector (radar interferometry-1, indoor measurement-2).

0	-1.8415	-0.401	0.8976
-0.7722	-1.2338	-0.3005	0.4122
-0.6916	-0.8696	-0.1329	0.1423
0	-0.6135	0.0644	0

Table 4.16. The displacements in the pixels of moving reflector, unit is cm (radar interferometry-1, indoor measurement-2).

0	-0.7988	-0.1739	0.3894
-0.335	-0.5352	-0.1303	0.1788
-0.3	-0.3772	-0.0576	0.0617
0	-0.2661	0.0279	0

4.4.2. Radar Interferometry-2

The reflector whose coordinates are $(-1, 3.5)$ is moved 1 cm to the left in the azimuth direction and the other reflector is kept steady. The schematic for the second interferometry measurements is given in Figure 4.41. VNA and antennas are calibrated

in 201 steps from 5 GHz to 6 GHz. Then results of interferometric phase values and displacements are received in Table 4.17 and 4.18. Since the movement in azimuth direction cannot be recognized by GB-SAR interferometry, results are parallel with experimental setup as expected.
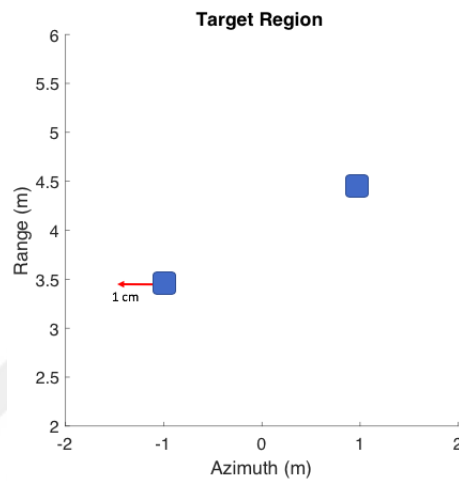
Figure 4.41. Schematic for radar interferometry-2, indoor measurement-2.

Figure 4.42. Master image-2 (indoor measurement-2), delay-and-sum algorithm, the pixel sizes are $5cm \times 5cm$, calibration is from 5 GHz to 6 GHz.

Figure 4.43. Slave image-2 (indoor measurement-2), delay-and-sum algorithm, the pixel sizes are $5cm \times 5cm$, calibration is from 5 GHz to 6 GHz.

Figure 4.44. Interferometric phases-2 (indoor measurement-2).

Table 4.17. Interferometric phase values of the pixels of moving reflector (radar interferometry-2, indoor measurement-2).

0.4886	0.3182	0.1403	0
0.7074	0.2814	0.0771	-0.3437
1.0211	0.2524	0.001	-0.3245
0	0.2251	-0.044	0

Table 4.18. The displacements in the pixels of moving reflector, unit is cm (radar interferometry-2, indoor measurement-2).

0.2119	0.138	0.0609	0
0.3068	0.1221	0.0334	-0.1491
0.4429	0.1095	0.0004	-0.1408
0	0.0976	-0.0191	0

4.4.3. Radar Interferometry-3

The reflector whose coordinates are $(-1, 3.5)$ is moved crosswise 1.5 cm (1 cm to the right in the azimuth direction, 1 cm towards the GB-SAR system in the range direction) and the other reflector is kept steady. The schematic for the third interferometry measurements is given in Figure 4.45. Then results of interferometric phase values and displacements are received in Table 4.19 and 4.20. There are displacements around 1 cm in the pixels of moving reflector and displacements increase from left to right because the movement in range direction can be recognized by GB-SAR interferometry. Results are parallel with experimental setup as expected.

Figure 4.45. Schematic for radar interferometry-3, indoor measurement-2.

Figure 4.46. Master image-3 (indoor measurement-2), delay-and-sum algorithm, the pixel sizes are $5cm \times 5cm$, calibration is from 5 GHz to 6 GHz.
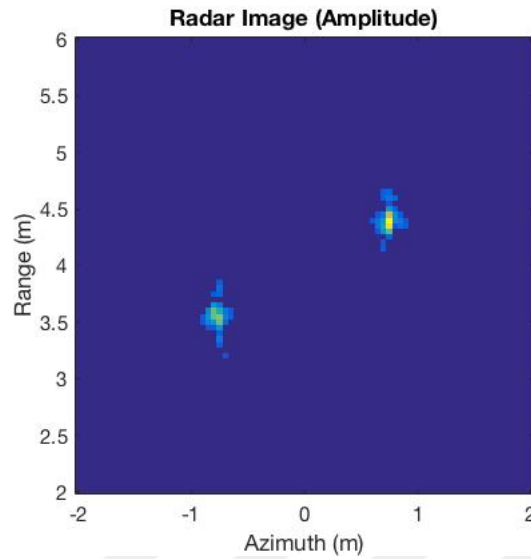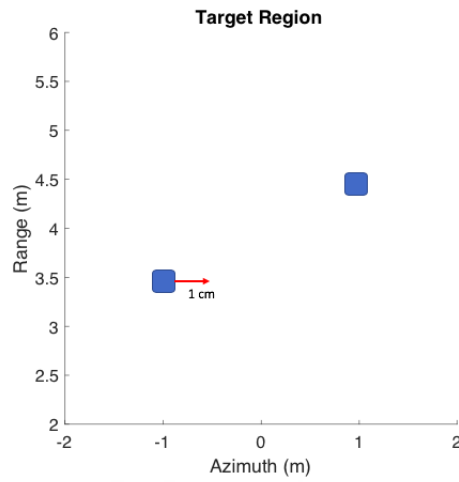

Figure 4.47. Slave image-3 (indoor measurement-2), delay-and-sum algorithm, the pixel sizes are $5cm \times 5cm$, calibration is from 5 GHz to 6 GHz.

Figure 4.48. Interferometric phases-3 (indoor measurement-2).

Table 4.19. Interferometric phase values of the pixels of the moving reflector (radar interferometry-3, indoor measurement-2).

0	1.9839	2.1952	2.3332
1.554	1.9153	2.1804	2.5088
1.5535	1.78	2.1613	2.788
0	1.6638	2.1365	0

Table 4.20. The displacements in the pixels of moving reflector, unit is cm (radar interferometry-3, indoor measurement-2).

0	0.8606	0.9522	1.0121
0.6741	0.8308	0.9458	1.0882
0.6739	0.7721	0.9375	1.2097
0	0.7217	0.9267	0

4.4.4. Radar Interferometry-4

The reflector whose coordinates are $(-1, 3.5)$ is moved crosswise 1.2 cm (8 mm to the left in the azimuth direction, 8 mm away from the GB-SAR system in the range direction) and the other reflector is kept steady. The schematic for the forth interferom-

etry measurements is given in Figure 4.49. Then results of interferometric phase values and displacements are received in Table 4.21 and 4.22. There are displacements around 8 mm in the pixels of moving reflector and displacements decrease from right to left because the movement in range direction can be recognized by GB-SAR interferometry. Results are parallel with experimental setup as expected.
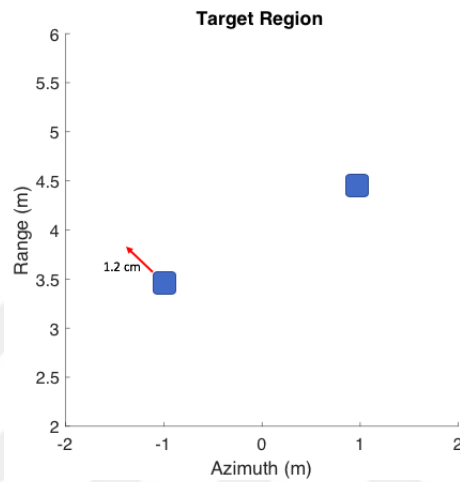
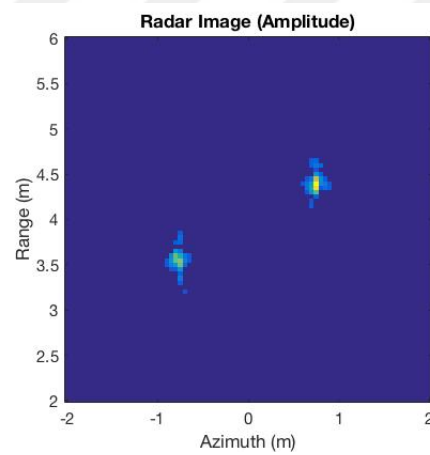Figure 4.49. Schematic for radar interferometry-4, indoor measurement-2.

Figure 4.50. Master image-4 (indoor measurement-2), delay-and-sum algorithm, the pixel sizes are $5cm \times 5cm$, calibration is from 5 GHz to 6 GHz.

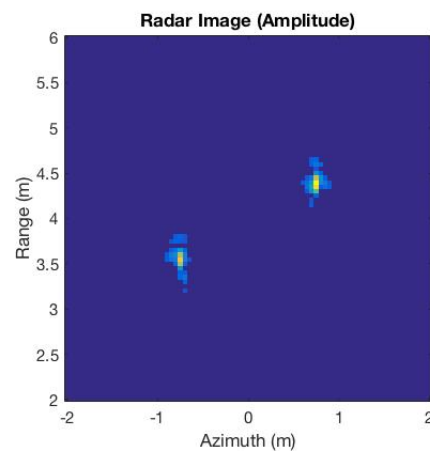Figure 4.51. Slave image-4 (indoor measurement-2), delay-and-sum algorithm, the pixel sizes are $5cm \times 5cm$, calibration is from 5 GHz to 6 GHz.
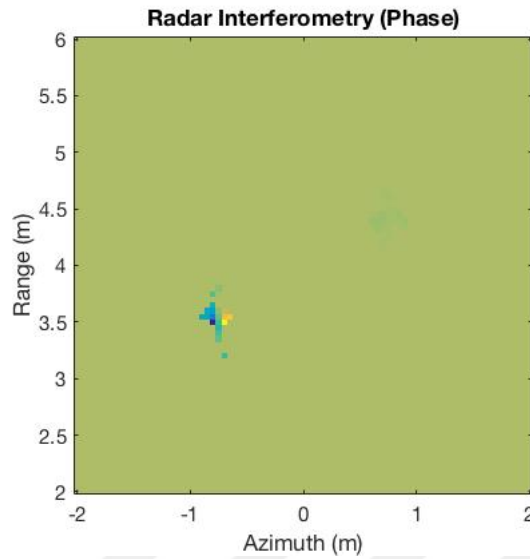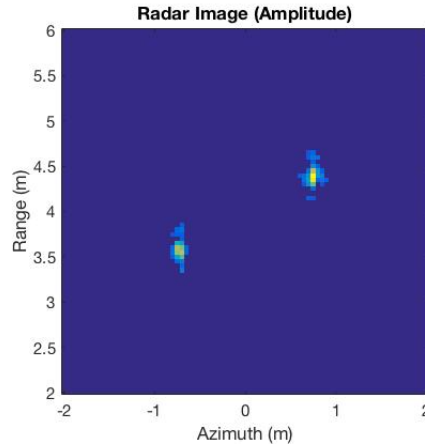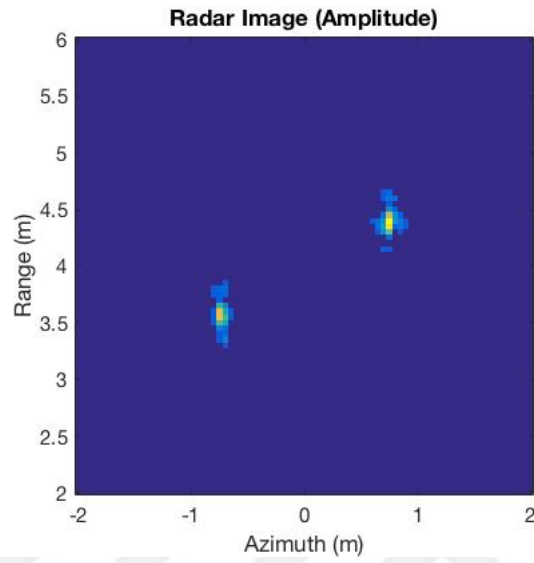

Figure 4.52. Interferometric phases-4 (indoor measurement-2).

Table 4.21. Interferometric phase values of the pixels of moving reflector (radar interferometry-4, indoor measurement-2).

-1.7821	-1.9249	-1.6193	0
-1.7779	-1.8235	-1.5904	-1.1921
-1.8524	-1.7535	-1.5473	-1.3214
-1.9448	-1.6884	-1.5024	-1.3441

Table 4.22. The displacements in the pixels of moving reflector, unit is cm (radar interferometry-4, indoor measurement-2).

-0.773	-0.835	-0.7024	0
-0.7712	-0.791	-0.6899	-0.5171
-0.8035	-0.7606	-0.6712	-0.5732
-0.8436	-0.7324	-0.6517	-0.583

4.5. Indoor Measurement-3

A metallic pipe, whose length is 1 meter, is located horizontally onto a reflector for the last indoor measurement. They are placed 5 meters across the center of the linear rail and the center of the rail is accepted as the origin, $(0,0)$, as mentioned before. These measurements are made to apply phase unwrapping algorithm.

Figure 4.53. Indoor measurement setup-3.

4.5.1. Radar Interferometry-1

After S_{21} parameters of the environment are collected, the metallic pipe is moved towards the GB-SAR system (the left limit of the metallic pipe is moved 3.5 cm towards the GB-SAR system, the center of the metallic pipe is moved 2 cm towards the GB-SAR system and the right limit of the metallic pipe is moved 0.5 cm towards the GB-SAR system) and S_{21} parameters of the environment are collected again, master and slave radar images are formed in Figure 4.55 and 4.56. The schematic for the first interferometry measurements is given in Figure 4.54. Then GB-SAR interferometry is found and initial interferometric phase values are received in Table 4.23. In Figure 4.58, column and row discontinuities between the pixels of the interferometric phase image are marked with arrows. End of the arrow indicates the small pixel value in the discontinuity pair. The discontinuity sum is 5.
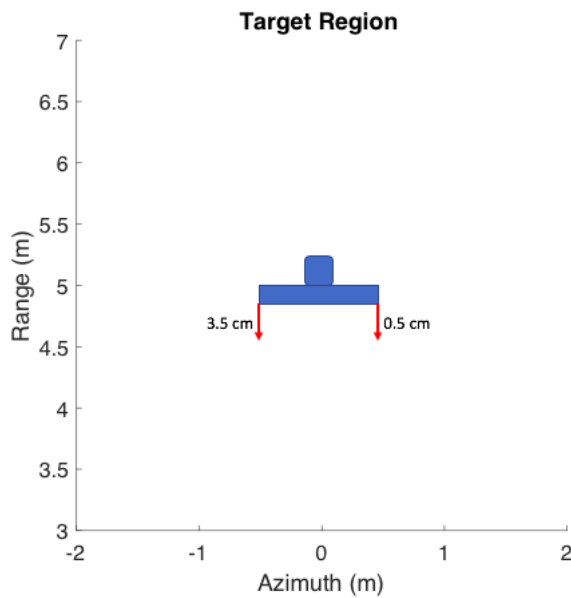
Figure 4.54. Schematic for radar interferometry-1, indoor measurement-3.
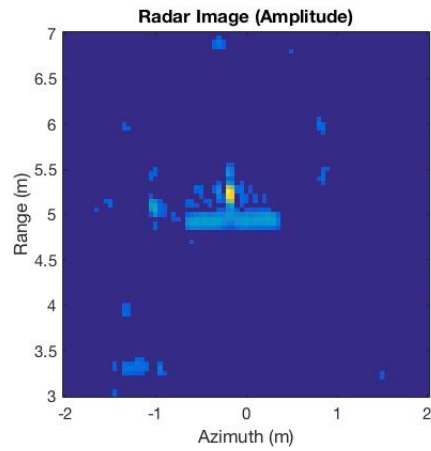
Figure 4.55. Master image-1 (indoor measurement-3), delay-and-sum algorithm, the pixel sizes are $5cm \times 5cm$, calibration is from 5 GHz to 6 GHz.
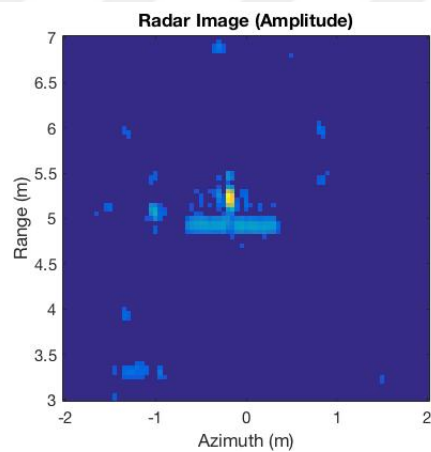
Figure 4.56. Slave image-1 (indoor measurement-3), delay-and-sum algorithm, the pixel sizes are $5cm \times 5cm$, calibration is from 5 GHz to 6 GHz.
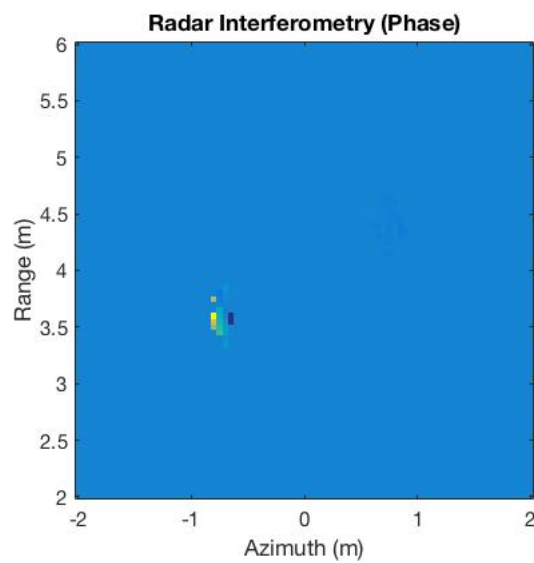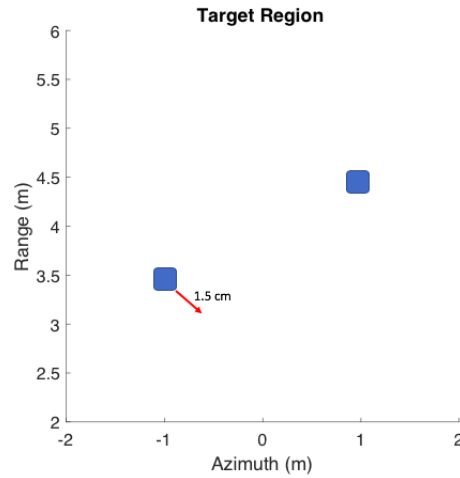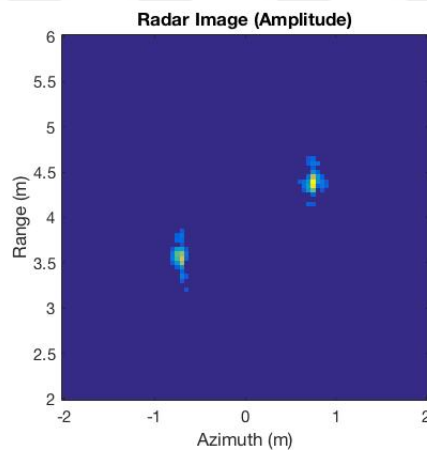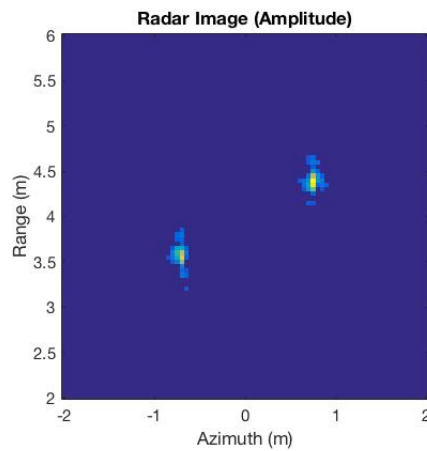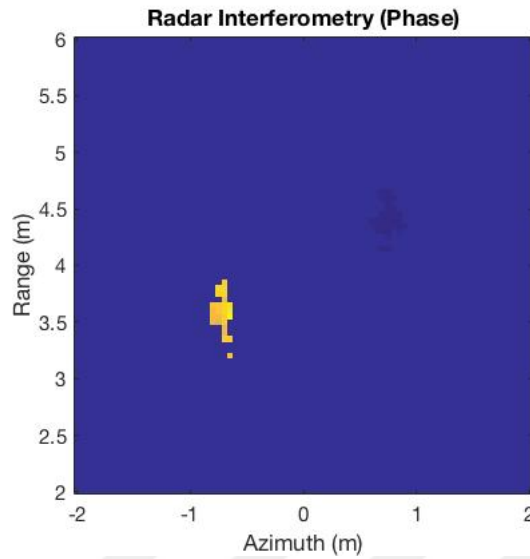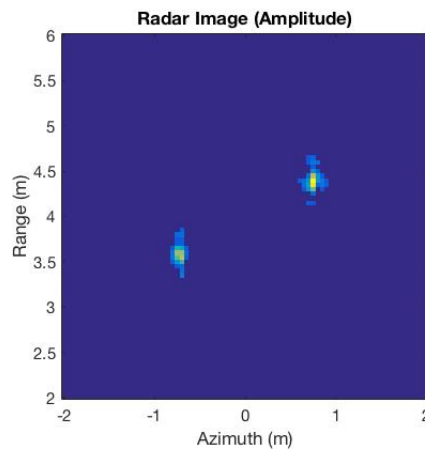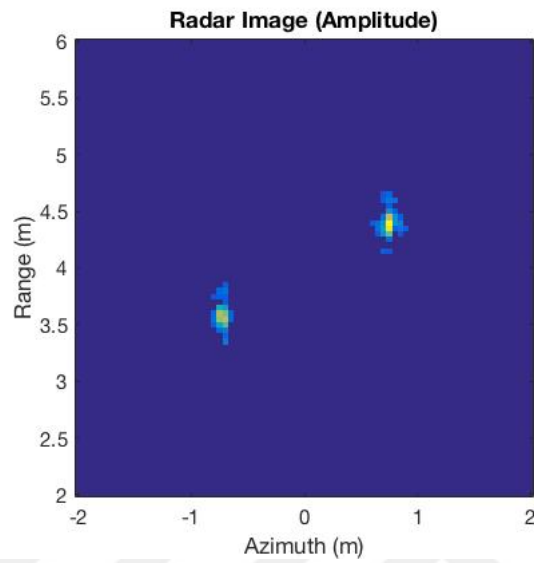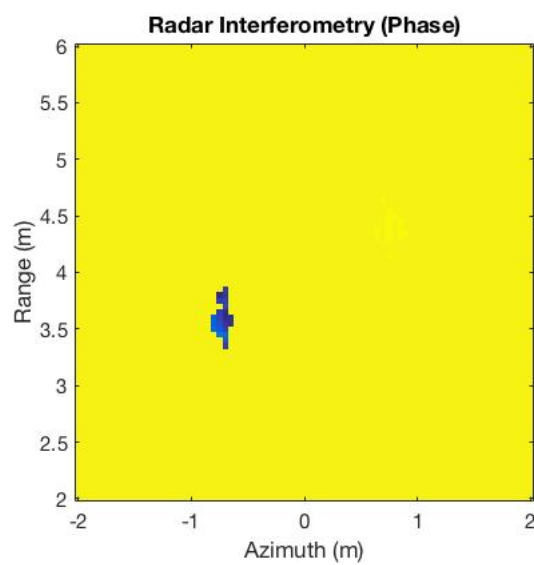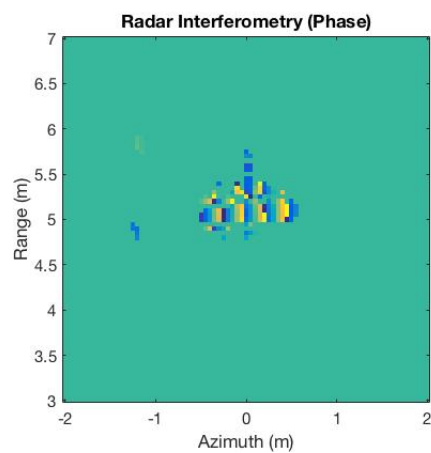

Figure 4.57. Interferometric phases-1 (indoor measurement-3).

Table 4.23. Initial interferometric phase values of the pixels of moving pipe (radar interferometry-1, indoor measurement-3).

1.7	1.6	1.5	1.2	0.7	0.3	-0.0	-0.4	-0.8	-1.7	-1.8	-1.6	-2.0	-2.2	-2.6	3.0	3.0	2.5	2.2	1.9	1.5
1.7	1.6	1.5	1.1	0.7	0.3	-0.0	-0.4	-0.8	-1.4	-1.8	-1.6	-2.0	-2.3	-2.7	3.1	3.0	2.5	2.2	1.8	1.6
1.9	1.7	1.4	1.1	0.7	0.3	-0.0	-0.4	-0.7	-1.0	-1.5	-1.6	-2.0	-2.4	-2.7	-3.1	3.0	2.4	2.1	1.7	1.5
2.1	1.7	1.4	1.0	0.7	0.3	-0.0	-0.3	-0.6	-0.6	-0.9	-1.6	-2.1	-2.5	-2.8	-3.1	3.0	2.4	2.0	1.7	0

```
1.7 1.6 1.5 1.2 0.7 0.3 -0.0 -0.4 -0.8 -1.7 -1.8 -1.6 -2.0 -2.2 -2.6❰3.0  3.0 2.5 2.2 1.9 1.5

1.7 1.6 1.5 1.1 0.7 0.3 -0.0 -0.4 -0.8 -1.4 -1.8 -1.6 -2.0 -2.3 -2.7❰3.1  3.0 2.5 2.2 1.8 1.6

1.9 1.7 1.4 1.1 0.7 0.3 -0.0 -0.4 -0.7 -1.0 -1.5 -1.6 -2.0 -2.4 -2.7 -3.1❰3.0 2.4 2.1 1.7 1.5

2.1 1.7 1.4 1.0 0.7 0.3 -0.0 -0.3 -0.6 -0.6 -0.9 -1.6 -2.1 -2.5 -2.8 -3.1❰3.0 2.4 2.0 1.7  0
```

Figure 4.58. Initial interferometric phase values of the pixels of moving pipe and marked discontinuities between pixels.

Then 2π is added to the small pixel values in all of the discontinuity pairs and the discontinuity sum becomes 5 and does not increase, so the interferometric phase values are updated. In Table 4.24, updated phase values of the pixels in the interferogram is given. Then the algorithm iterates the procedure over the updated interferometric phases and the next search starts. In Figure 4.59, column and row discontinuities are marked between the pixels of the updated interferometric phase image. Then 2π is added to the small pixel values in all of the discontinuity pairs and updated phase values of the pixels in the interferogram is given in Table 4.25.

Table 4.24. Interferometric phase values of the pixels of moving pipe after the first search.

1.7	1.6	1.5	1.2	0.7	0.3	-0.0	-0.4	-0.8	-1.7	-1.8	-1.6	-2.0	-2.2	3.7	3.0	3.0	2.5	2.2	1.9	1.5
1.7	1.6	1.5	1.1	0.7	0.3	-0.0	-0.4	-0.8	-1.4	-1.8	-1.6	-2.0	-2.3	3.6	3.1	3.0	2.5	2.2	1.8	1.6
1.9	1.7	1.4	1.1	0.7	0.3	-0.0	-0.4	-0.7	-1.0	-1.5	-1.6	-2.0	-2.4	-2.7	3.2	3.0	2.4	2.1	1.7	1.5
2.1	1.7	1.4	1.0	0.7	0.3	-0.0	-0.3	-0.6	-0.6	-0.9	-1.6	-2.1	-2.5	-2.8	3.2	3.0	2.4	2.0	1.7	0

1.7 1.6 1.5 1.2 0.7 0.3 -0.0 -0.4 -0.8 -1.7 -1.8 -1.6 -2.0 -2.2◄3.7 3.0 3.0 2.5 2.2 1.9 1.5

1.7 1.6 1.5 1.1 0.7 0.3 -0.0 -0.4 -0.8 -1.4 -1.8 -1.6 -2.0 -2.3◄3.6 3.1 3.0 2.5 2.2 1.8 1.6

1.9 1.7 1.4 1.1 0.7 0.3 -0.0 -0.4 -0.7 -1.0 -1.5 -1.6 -2.0 -2.4 -2.7◄3.2 3.0 2.4 2.1 1.7 1.5

2.1 1.7 1.4 1.0 0.7 0.3 -0.0 -0.3 -0.6 -0.6 -0.9 -1.6 -2.1 -2.5 -2.8◄3.2 3.0 2.4 2.0 1.7 0

Figure 4.59. Interferometric phase values of the pixels of moving pipe after the first search and marked discontinuities between pixels.

Table 4.25. Interferometric phase values of the pixels of moving pipe after the second search.

1.7	1.6	1.5	1.2	0.7	0.3	-0.0	-0.4	-0.8	-1.7	-1.8	-1.6	-2.0	4.1	3.7	3.0	3.0	2.5	2.2	1.9	1.5
1.7	1.6	1.5	1.1	0.7	0.3	-0.0	-0.4	-0.8	-1.4	-1.8	-1.6	-2.0	4.0	3.6	3.1	3.0	2.5	2.2	1.8	1.6
1.9	1.7	1.4	1.1	0.7	0.3	-0.0	-0.4	-0.7	-1.0	-1.5	-1.6	-2.0	-2.4	3.6	3.2	3.0	2.4	2.1	1.7	1.5
2.1	1.7	1.4	1.0	0.7	0.3	-0.0	-0.3	-0.6	-0.6	-0.9	-1.6	-2.1	-2.5	3.5	3.2	3.0	2.4	2.0	1.7	0

In Table 4.26, final phase values of the pixels in the interferogram can be seen. The phase unwrapping algorithm terminates when all of the discontinuities are removed. After the last search is over, the discontinuity sum is 0. The interferometric phases can be translated into the displacements by using equation 3.2 or equation 3.4. Displacement results are received in Table 4.27 and results are parallel with experimental setup as expected.

Table 4.26. Final interferometric phase values of the pixels of moving pipe after phase unwrapping (radar interferometry-1, indoor measurement-3).

8.0	7.9	7.7	7.4	7.0	6.6	6.3	6.0	5.5	4.6	4.5	4.6	4.3	4.1	3.7	3.0	3.0	2.5	2.2	1.9	1.5
8.0	7.9	7.7	7.4	7.0	6.6	6.3	5.9	5.5	4.9	4.5	4.6	4.3	4.0	3.6	3.1	3.0	2.5	2.2	1.8	1.6
8.1	7.9	7.7	7.4	7.0	6.6	6.3	5.9	5.6	5.2	4.8	4.6	4.3	3.9	3.6	3.2	3.0	2.4	2.1	1.7	1.5
8.4	8.0	7.6	7.3	7.0	6.6	6.3	5.9	5.7	5.6	5.4	4.7	4.2	3.8	3.5	3.2	3.0	2.4	2.0	1.7	0

Table 4.27. Displacements in the the pixels of moving pipe after phase unwrapping, unit is cm(radar interferometry-1, indoor measurement-3).

3.4	3.4	3.3	3.2	3.0	2.8	2.7	2.6	2.4	2.0	1.9	2.0	1.8	1.8	1.6	1.3	1.3	1.1	1.0	0.8	0.7
3.5	3.4	3.3	3.2	3.0	2.8	2.7	2.6	2.4	2.1	1.9	2.0	1.9	1.7	1.6	1.4	1.3	1.1	0.9	0.8	0.7
3.5	3.4	3.3	3.2	3.0	2.8	2.7	2.6	2.4	2.3	2.1	2.0	1.8	1.7	1.5	1.4	1.3	1.0	0.9	0.7	0.7
3.6	3.5	3.3	3.1	3.0	3.0	2.7	2.6	2.4	2.4	2.3	2.0	1.8	1.6	1.5	1.4	1.3	1.0	0.9	0.7	0

4.5.2. Radar Interferometry-2

After S_{21} parameters of the environment are collected, the metallic pipe is moved (the left limit of the metallic pipe is moved 1 cm away from the GB-SAR system, the center of the metallic pipe is moved 5.5 cm towards the GB-SAR system and the right limit of the metallic pipe is moved 10 cm towards the GB-SAR system) and S_{21} parameters of the environment are collected again, master and slave radar images are formed in Figure 4.61 and 4.62. The schematic for the second interferometry measurements is given in Figure 4.60. Then GB-SAR interferometry is found and initial interferometric phase values are received in Table 4.28. In Figure 4.64, column and row discontinuities between the pixels of the interferometric phase image are marked with arrows.
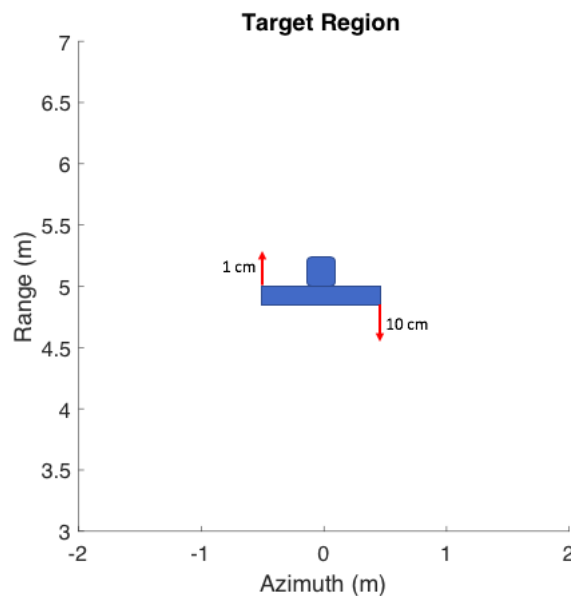
Figure 4.60. Schematic for radar interferometry-2, indoor measurement-3.

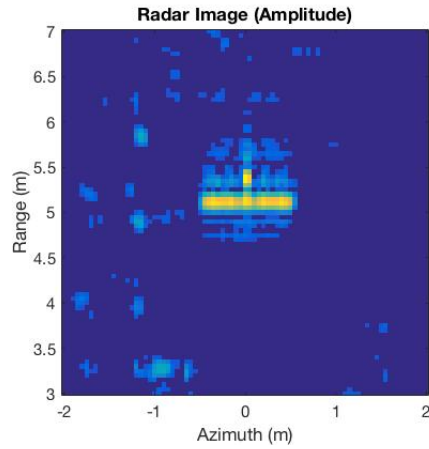Figure 4.61. Master image-2 (indoor measurement-3), delay-and-sum algorithm, the pixel sizes are $5cm \times 5cm$, calibration is from 5 GHz to 6 GHz.
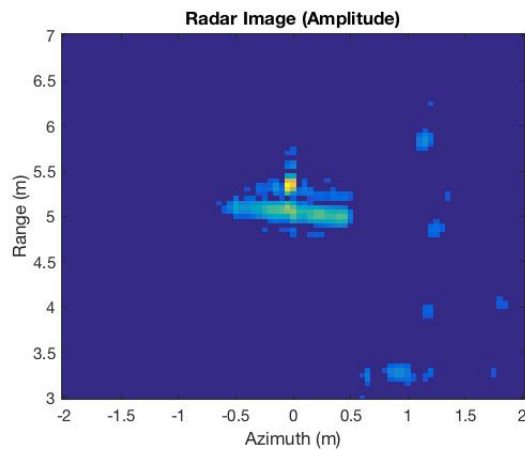
Figure 4.62. Slave image-2 (indoor measurement-3), delay-and-sum algorithm, the pixel sizes are $5cm \times 5cm$, calibration is from 5 GHz to 6 GHz.
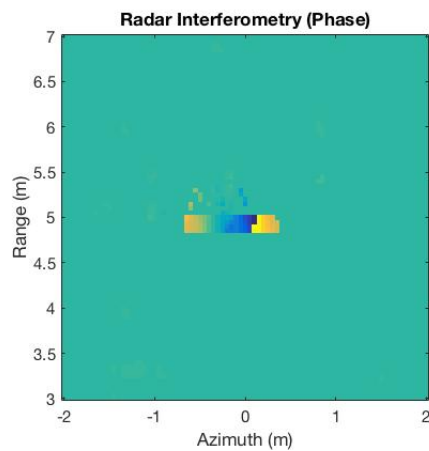
Figure 4.63. Interferometric phases-2 (indoor measurement-3).

Table 4.28. Initial interferometric phase values of the pixels of moving pipe (radar interferometry-2, indoor measurement-3).

-2.8	-2.2	-1.1	0.5	1.7	-3.0	-1.7	-0.3	1.0	2.6	-2.1	-1.0	0.2	1.6	2.9	-2.0	-0.6	0.8	2.0	-3.1	-2.2	0
-2.8	-2.2	-1.1	0.4	1.8	-3.1	-1.7	-0.3	0.9	2.4	-2.4	-1.2	0.2	1.6	3.1	-1.9	-0.6	0.8	2.0	3.1	-2.3	-1.5
0	-2.1	-1.0	0.5	1.9	-3.1	-1.7	-0.4	1.0	2.3	-2.2	-1.2	0.3	1.6	-3.1	-1.9	-0.6	0.8	2.0	3.0	-2.3	-1.6
0	0	0	0	0	0	0	-0.5	1.3	2.3	-1.9	-1.2	0.4	1.7	-3.0	-1.7	-0.4	0.8	2.1	3.1	-2.3	-1.6

Figure 4.64. Initial interferometric phase values of the pixels of moving pipe marked discontinuities between pixels.

After phase unwrapping is applied to interferometric phase image and the last search is over, the phase values of the pixels in 6th column, 7th column, 8th column, 9th column and 10th column are increased by 2π, the phase values of the pixels from 11th column to 15th column are increased by 4π, multiple of 2π, the phase values of the pixels from 16th column to 19th column are increased by 6π and the phase values of the pixels from 20th column to 22th column are increased by 8π. In Table 4.29, final phase values of the pixels in the interferogram can be seen and the discontinuity sum is 0. Displacement results are received in Table 4.30 and results are parallel with experimental setup as expected.

Table 4.29. Final interferometric phase values of the pixels of moving pipe after phase unwrapping (radar interferometry-2, indoor measurement-3).

-2.8	-2.2	-1.1	0.5	1.7	3.2	4.5	5.9	7.2	8.8	10.4	11.6	12.8	14.1	15.5	16.8	18.2	19.7	20.9	22.0	22.9	0
-2.8	-2.2	-1.1	0.4	1.8	3.1	4.5	5.9	7.1	8.6	10.2	11.4	12.8	14.2	15.6	16.9	18.2	19.6	20.8	21.9	22.8	23.6
0	-2.1	-1.0	0.5	1.9	3.1	4.5	5.8	7.2	8.5	10.3	11.3	12.9	14.2	15.7	17.0	18.3	20.0	20.9	21.9	22.8	23.6
0	0	0	0	0	0	0	5.7	7.5	8.5	10.7	11.4	13.0	14.3	15.8	17.1	18.4	19.7	21.0	21.9	22.8	23.5

Table 4.30. Displacements in the the pixels of moving pipe after phase unwrapping, unit is cm(radar interferometry-2, indoor measurement-3).

-1.2	-1.0	-0.5	0.2	0.7	1.4	2.0	2.6	3.1	3.8	4.5	5.0	5.5	6.1	6.7	7.2	7.8	8.5	9.0	9.4	9.8	0
-1.2	-1.0	-0.5	0.2	0.8	1.4	2.0	2.6	3.1	3.7	4.4	4.9	5.5	6.1	6.7	7.3	7.8	8.4	9.0	9.4	9.8	10.2
0	-0.9	-0.4	0.2	0.8	1.4	2.0	2.5	3.1	3.7	4.4	4.9	5.5	6.1	6.8	7.3	7.9	8.4	9.0	9.4	9.8	10.1
0	0	0	0	0	0	0	2.5	3.2	3.7	4.6	4.9	5.6	6.1	6.8	7.4	7.9	8.5	9.0	9.4	9.8	10.1

4.6. A Study on Phase Unwrapping Algorithm

In this section, a wrapped interferometric phase image, 100×100 matrix, is prepared to test the robustness and performance of the developed 2D phase unwrapping algorithm. The wrapped interferometric phase image is given in Figure 4.65.
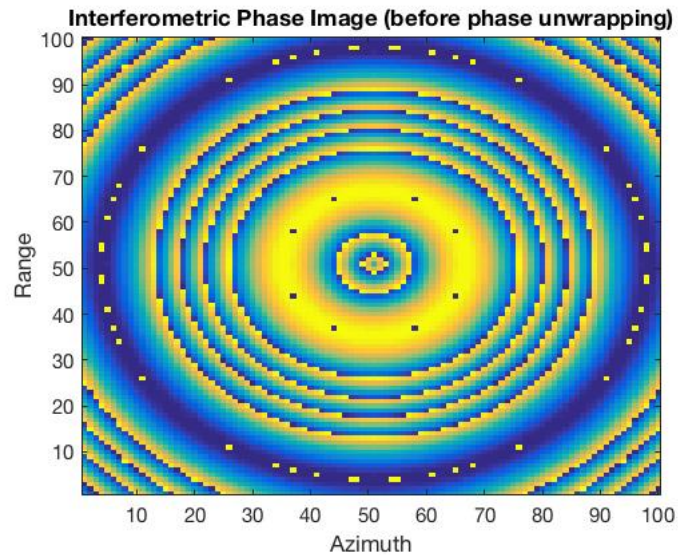
Figure 4.65. Wrapped interferometric phase image.

After 2D phase unwrapping algorithm is applied on the wrapped interferometric phase image, all of the discontinuities are removed and the discontinuity sum is reduced to zero. The unwrapped interferometric phase image is given in Figure 4.66.
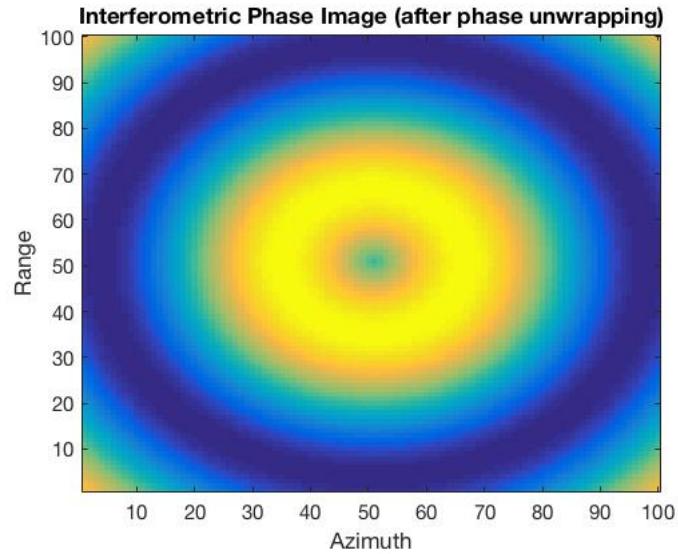
Figure 4.66. Unwrapped interferometric phase image.

Then uniformly distributed random numbers in the interval $(-\epsilon, \epsilon)$ are added to the wrapped interferometric phase image and Monte Carlo simulations are run on the interferometric phases to test the performance of the phase unwrapping algorithm. If ϵ is less than 0.8, the algorithm prints out the true final interferometric phase image and all of the discontinuities are still removed in every simulation. If ϵ is more than 0.9, the phase unwrapping algorithm fails in every simulation. Results can be seen in Figure 4.67.
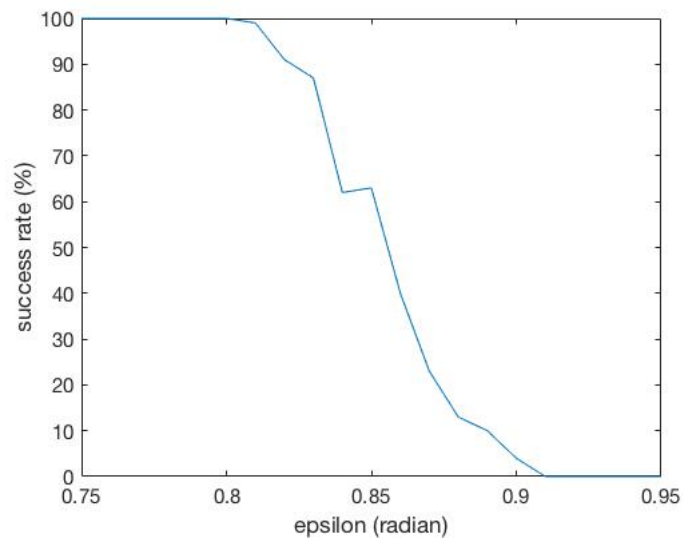
Figure 4.67. Performance of the phase unwrapping algorithm.

Simulation results show that the method is robust and gives out the true interferometric phase image even though local errors around $\pi/2$ are formed between two consecutive interferometric phases.
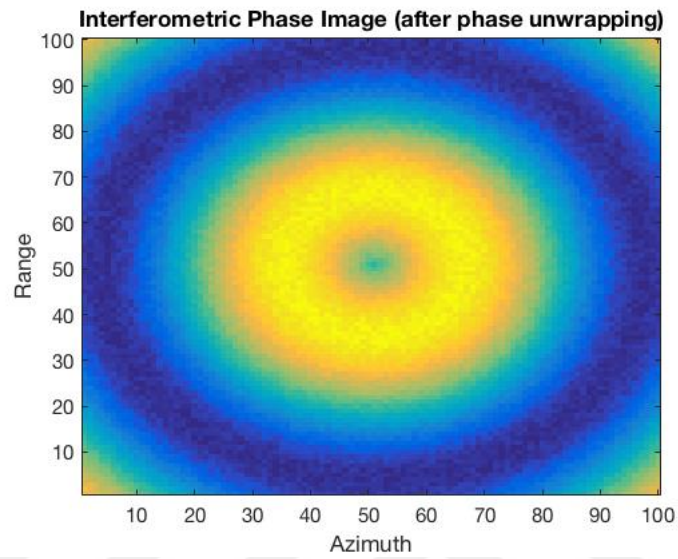
Figure 4.68. Unwrapped interferometric phase image, $\epsilon = \pi/4$.

5. CONCLUSION

In this study, a GB-SAR system is designed to collect the experimental data of the target region, form indoor and outdoor two dimensional radar images, compare two radar images received at different times and detect potential changes and movements of the objects by using radar interferometry.

The GB-SAR platform consists of a computer, a transmitting antenna, a receiving antenna and VNA and is located onto the linear rail. The code for controlling the movement of the rail was already implemented and I implemented another code to control both the rail and the VNA at the same time. After VNA collects the S_{21} parameters of the environment and sends to the computer, the radar platform, which is at the beginning of the rail, moves 20 mm in azimuth direction and the VNA repeats the same procedure. This process continues until the platform reaches to the end of the rail. Experimental data of the different indoor and outdoor environments are collected several times by using this GB-SAR system to monitor the target region.

Then 2D GB-SAR images of indoor and outdoor target regions are formed by using experimental data by applying two different methods. Radar images of all of the measurements in chapter 4 show the success of the methods, the radar image results are parallel with the experimental setup. I prepared a paper for a novel 2D GB-SAR imaging and signal processing algorithm and the paper got accepted in ICECS'19, Sarajevo (International Conference on Electrical Engineering and Computer Science). My proposed algorithm is an accomplished solution to monitor small target regions in close ranges. Also, a well-known and widely-used method, delay-and-sum algorithm, is implemented and applied for 2D radar imaging and GB-SAR interferometry.

GB-SAR interferometry is used to compare two radar images of the same target region, detect changes and calculate the displacements of the objects in this study but 2D phase unwrapping algorithm must be applied to detect the true changes and

displacements in the interferometric phase image because the interferometric phases are measured modulo 2π and differ from $-\pi$ to π, so the phases need elevations to monitor displacements larger than $(\frac{\lambda_c}{4\pi}\pi)$ in the pixels. Phase is continuous, so the interferometric phase difference between two neighbouring pixels should be less than π, otherwise it is a discontinuity and discontinuities should be eliminated to reach the true profile. Therefore, I implemented a novel phase unwrapping algorithm to remove discontinuities in the interferometric phase image. After my proposed phase unwrapping algorithm is applied to the phase results of radar interferometry-1 and radar interferometry-2 of the last indoor measurement in chapter 4, total sum of the discontinuities is reduced to zero in the final interferometric phase images and then the true interferometric phases and the actual displacements in the pixels are calculated. The final interferometric phase images and calculated displacements are parallel with the experimental setup and results prove that phase unwrapping is necessary for GB-SAR interferometry. Also, the robustness and performance of the proposed phase unwrapping algorithm are proven in the last section of chapter 4.

Atmospheric delay and instrumental instability affect the phases and displacement calculations in GB-SAR interferogram. To correct measured phases and displacements, a steady reflector is located as a reference point in the target region during the measurements and the range-independent variable, β_φ, is calculated since the target regions are in close ranges. My literature survey about GB-SAR interferometry shows that atmospheric and instrumental correction (calculating both the range-dependent variable, $(\alpha_f + \epsilon_{atm})$, and the range-independent variable, β_φ) is very important and needed to be applied to interferogram results in distant ranges.

This study shows the success of GB-SAR interferometry to compare two radar images, which are taken at different times, and then detect changes and monitor displacements in the range direction. The phase information of a pixel in the interferogram is directly related to the displacement in the range direction. After the radar parameters of the environment is collected and the master image is formed, one of the objects is moved in several directions and then the radar parameters of the environment is

collected and slave image is formed. After master and slave images are retrieved, interferometric phase image is constructed. One of the objects is moved in range direction in outdoor measurement-2 and indoor measurement-1. The interferometric phases and displacement results are parallel with the experimental setup and prove that displacement in the range direction can be detected and calculated by GB-SAR interferometry. One of the objects is moved in azimuth direction for radar interferometry-1 and radar interferometry-2 in the second indoor measurement. The interferometric phases and displacement results are parallel with the experimental setup and prove that the movement of the object in azimuth direction cannot be recognized by GB-SAR interferometry. One of the objects is moved crosswise for radar interferometry-3 and radar interferometry-4 in the second indoor measurement. The interferometric phases and displacement results are parallel with the experimental setup and prove that GB-SAR interferometry detects the amount of the displacement just only in the range direction if the object is moved crosswise. Centre frequency or centre wavelength determines the ratio between the interferometric phase of a pixel and the displacement in the pixel. VNA and antennas are calibrated from 5 GHz to 6 GHz for radar interferometry-1 and they are calibrated from 4 GHz to 5 GHz for radar interferometry-2 in the first indoor measurement and the same movement is analyzed. The displacements results are very close and parallel with the experimental setup although different calibration intervals are used. Also, the pixel size is selected as $2cm \times 2cm$ and the target region is determined as $4m \times 5m$ in radar interferometry-4 of the first indoor measurement. The interferometric phase image and the calculated displacements show the direct dependency between the interferometric phase and the displacement in the range direction is still valid.

In this study, a GB-SAR system designed and its data collection method is expressed. 2D SAR imaging algorithms with collected radar parameters are identified and a novel 2D GB-SAR imaging algorithm is compared with one of the most widely-used method. Then radar interferometry is explained to detect changes and a 2D phase unwrapping algorithm is proposed to reach the true phases and the actual displacements. In other words, an application of GB-SAR interferometry is discussed in this study.

Results and researches show that the proposed method on GB-SAR interferometry is a satisfying alternative to spaceborne and airborne SAR and these methods are valid to form radar interferometry of large target regions and detect changes in distant ranges.

REFERENCES

1. M. Soumekh (1999), *Synthetic aperture radar signal processing with MATLAB algorithms.* New York: John Wiley, 249-261.

2. A. Moreira, P. Prats-Iraola, M. Younis, G. Krieger, I. Hajnsek and K. P. Papathanassiou, "A tutorial on synthetic aperture radar," in *IEEE Geoscience and Remote Sensing Magazine*, vol. 1, no. 1, pp. 6-43, March 2013.

3. Zebker, H. A., Rosen, P. A., Goldstein, R. M., Gabriel, A., and Werner, C. L. (1994), *On the derivation of coseismic displacement fields using differential radar interferometry: The Landers earthquake*, J. Geophys. Res., 99(B10), 19617-19634.

4. H. A. Zebker and J. Villasenor, "Decorrelation in interferometric radar echoes," in *IEEE Transactions on Geoscience and Remote Sensing*, vol. 30, no. 5, pp. 950-959, Sept. 1992.

5. M. Costantini and P. A. Rosen, "A generalized phase unwrapping approach for sparse data," *IEEE 1999 International Geoscience and Remote Sensing Symposium. IGARSS'99 (Cat. No.99CH36293)*, Hamburg, Germany, 1999, pp. 267-269 vol.1.

6. Thomas J. Flynn, "*Two-dimensional phase unwrapping with minimum weighted discontinuity*," J. Opt. Soc. Am. A 14, 2692-2701 (1997).

7. A. Ferretti, C. Prati and F. Rocca, "Analysis of Permanent Scatterers in SAR interferometry," IGARSS 2000. *IEEE 2000 International Geoscience and Remote Sensing Symposium. Taking the Pulse of the Planet: The Role of Remote Sensing in Managing the Environment. Proceedings (Cat. No.00CH37120)*, Honolulu, HI, USA, 2000, pp. 761-763 vol.2.

8. T. K. Sarkar and M. S. Palma, "A history of Evolution of Radar," in *Proceedings*

Of The 44th European Microwave Conference, Rome, 2014.

9. D. Ghose, "Principles of Radars," in *Navigation, Guidance and Control*, Bangalore, NPTEL COURSE, 2012, pp. 4-9.

10. M. I. Skolnik, "Radar Transmitter," in *Introduction To Radar Systems*, Singapore, McGraw-Hill Book Company, 1980, pp. 190-192.

11. "IEEE Standard Letter Designations For Radar-Frequency Bands," *IEEE Std 521-2002 (Revision of IEEE Std 521-1984)*, pp. 1-3, 2003.

12. C. Wolff, "*Radar Basics*," 17 November 1998. [Online]. Available: http://www.radartutorial.eu/07.waves/Waves%20and%20Frequency%20Ranges.en.html., accessed in October 2019.

13. C. Wolff, "*Radar Basics*," 17 November 1998. [Online]. Available: http://www.radartutorial.eu/01.basics/The%20Radar%20Range%20Equation.en.html., accessed in October 2019.

14. C. Wolff, "*Radar Basics*," 17 November 1998. [Online]. Available: http:/www.rfcafe.com/references/electrical/ew-radar-handbook/radar-cross-section.htm., accessed in October 2019.

15. C. Wolff, "*Radar Basics*," 17 November 1998. [Online]. Available: https://www.microwaves101.com/encyclopedias/corner-reflectors., accessed in October 2019.

16. T. Jin, H. Wang and H. Liu, "Design of a flexible high-performance real-time SAR signal processing system," *2016 IEEE 13th International Conference on Signal Processing (ICSP)*, Chengdu, 2016, pp. 513-517.

17. B. Omuz, F. Öz, Ö. Özdemir and A. Öncü, "Experimental Verification of In-door Ground Based SAR Using Beam Space MUSIC Algorithm," *2018 International*

Conference on Electromagnetics in Advanced Applications (ICEAA), Cartagena des Indias, 2018, pp. 213-216.

18. Walter G. Carrara, Ronald M. Majewski, Ron S. Goodman, *Spotlight Synthetic Aperture Radar Signal Processing Algorithms*, London: Artech House Remote Sensing Library, 1995.

19. P. R. Johnston and R. M. Gulrajani, "Selecting the corner in the L-curve approach to Tikhonov regularization," in *IEEE Transactions on Biomedical Engineering*, vol. 47, no. 9, pp. 1293-1296, Sept. 2000.

20. L. Ying, D. Xu and Z. -. Liang, "On Tikhonov regularization for image reconstruction in parallel MRI," *The 26th Annual International Conference of the IEEE Engineering in Medicine and Biology Society*, San Francisco, CA, 2004, pp. 1056-1059.

21. L. Noferini et al., "Permanent scatterers analysis for atmospheric correction in ground-based SAR interferometry," in *IEEE Transactions on Geoscience and Remote Sensing*, vol. 43, no. 7, pp. 1459-1471, July 2005.

22. Massonnet, D., and Feigl, K. L. (1998), *Radar interferometry and its application to changes in the Earth's surface*, Rev. Geophys., 36(4), 441- 500.

23. Zebker, H. A., Rosen, P. A., and Hensley, S. (1997), *Atmospheric effects in interferometric synthetic aperture radar surface deformation and topographic maps*, J. Geophys. Res., 102(B4), 7547-7563.

24. R. M. Goldstein, H. A. Zebker and C. L. Werner, "Satellite radar interferometry: Two-dimensional phase unwrapping," in *Radio Science*, vol. 23, no. 4, pp. 713-720, July-Aug. 1988.

25. G. Luzi et al., "Ground-based radar interferometry for landslides monitoring: atmospheric and instrumental decorrelation sources on experimental data," in *IEEE*

Transactions on Geoscience and Remote Sensing, vol. 42, no. 11, pp. 2454-2466, Nov. 2004.

26. D. Leva, G. Nico, D. Tarchi, J. Fortuny-Guasch and A. J. Sieber, "Temporal analysis of a landslide by means of a ground-based SAR Interferometer," in *IEEE Transactions on Geoscience and Remote Sensing*, vol. 41, no. 4, pp. 745-752, April 2003.